

Chemical differences among collapsing low-mass protostellar cores

Jingfei Sun¹, Xiaohu Li^{1,2}, Fujun Du^{3,4}, Yao Wang³, Juan Tuo^{1,5}, Yanan Feng^{1,5}

¹ Xinjiang Astronomical Observatory, Chinese Academy of Sciences, 150 Science 1-Street, Urumqi 830011, P.R.China
e-mail: sunjingfei@xao.ac.cn; xiaohu.li@xao.ac.cn

² Key Laboratory of Radio Astronomy, Chinese Academy of Sciences, Urumqi 830011, P.R.China

³ Purple Mountain Observatory and Key Laboratory of Radio Astronomy, Chinese Academy of Sciences, Nanjing 210023, P.R.China

⁴ School of Astronomy and Space Science, University of Science and Technology of China, Hefei 230026, P.R.China

⁵ University of Chinese Academy of Sciences, P.R.China

Received XXX; accepted XXX

ABSTRACT

Context. Organic features lead to two distinct types of Class 0/I low-mass protostars: hot corino sources, exhibiting abundant saturated complex organic molecules (COMs), and warm carbon-chain chemistry (WCCC) sources, exhibiting abundant unsaturated carbon-chain molecules. Some observations suggest that the chemical variations between WCCC sources and hot corino sources are associated with local environments, as well as the luminosity of protostars.

Aims. We aim to investigate the physical conditions that significantly affect WCCC and hot corino chemistry, and to reproduce the chemical characteristics of prototypical WCCC sources and hybrid sources, where both carbon-chain molecules and COMs are abundant.

Methods. We conducted gas-grain chemical simulation in collapsing protostellar cores, adopting some typical physical parameters for the fiducial model. By changing values of some physical parameters, including the visual extinction of ambient clouds (A_V^{amb}), the cosmic-ray ionization rate (ζ), the maximum temperature during the warm-up phase (T_{max}), and the contraction timescale of protostars (t_{cont}), we studied the dependence of WCCC and hot corino chemistry on these physical parameters. Subsequently, we ran a model with different physical parameters to reproduce scarce COMs in prototypical WCCC sources.

Results. The fiducial model predicts abundant carbon-chain molecules and COMs, and reproduces WCCC and hot corino chemistry in the hybrid source L483. This suggests that WCCC and hot corino chemistry can coexist in some hybrid sources. Ultraviolet (UV) photons and cosmic rays can boost WCCC features by accelerating the dissociation of CO and CH₄ molecules. On the other hand, UV photons can weaken the hot corino chemistry by photodissociation reactions, while the dependence of hot corino chemistry on cosmic rays is relatively complex. The T_{max} does not affect WCCC features, while it can influence hot corino chemistry by changing the effective duration of two-body surface reactions for most COMs. The long t_{cont} can boost WCCC and hot corino chemistry, by prolonging the effective duration of WCCC reactions in the gas phase and surface formation reactions for COMs, respectively. The scarcity of COMs in prototypical WCCC sources can be explained by insufficient dust temperature in the inner envelopes to activate hot corino chemistry. Meanwhile, the High ζ and the long t_{cont} favors the explanation for scarce COMs in these sources.

Conclusions. The chemical differences between WCCC sources and hot corino sources can be attributed to the variations in local environments, such as A_V^{amb} , ζ , as well as the protostellar property t_{cont} .

Key words. Astrochemistry – Stars: protostars – ISM: abundances – ISM: evolution – ISM: clouds – ISM: molecules

1. Introduction

Carbon-bearing molecules consisting of six or more atoms are considered as complex organic molecules (COMs, Herbst & van Dishoeck 2009; Jørgensen et al. 2020; Ceccarelli et al. 2023), and some of them suggest a possible relation between interstellar chemistry and the emergence of life on Earth. COMs have been detected in many objects, including prestellar or starless cores (e.g., Jiménez-Serra et al. 2016; Scibelli et al. 2021), protostellar cores (e.g., Chahine et al. 2022), protostellar disks (e.g., Lee et al. 2019), and protoplanetary disks (e.g., Loomis et al. 2018). The chemistry in low-mass protostellar cores is a main topic of astronomy, as it determines the interstellar chemical legacy inherited by protoplanetary disks. During the early phases of low-mass protostellar cores, namely Class 0 and I, organic characteristics lead to two special types of protostars: hot corinos (e.g., Cazaux et al. 2003; Ceccarelli et al. 2017) and warm carbon-

chain chemistry sources (WCCC; e.g., Sakai et al. 2008; Hirota et al. 2009).

Hot corinos are compact sources (with sizes ≤ 100 au) with high temperatures (≥ 100 K), showing abundant presence of saturated COMs in hot central regions (e.g., van Dishoeck et al. 1995; Ceccarelli 2004; Caux et al. 2011; Taquet et al. 2015; Jørgensen et al. 2016; López-Sepulcre et al. 2017). Currently, more than twenty COMs (e.g., CH₃OH, CH₃CN, CH₃OCH₃, NH₂CHO, etc.) have been detected in hot corinos (Imai et al. 2016; Jørgensen et al. 2016; López-Sepulcre et al. 2017; Marcelino et al. 2018b; Bianchi et al. 2019; Belloche et al. 2020; Nazari et al. 2021; Chahine et al. 2022). The first detected hot corino was in IRAS16293-2422 (referred to as IRAS16293; Cazaux et al. 2003), which contains two hot corinos, A and B (Kuan et al. 2004; Bottinelli et al. 2004b). Later, other hot corinos were found towards NGC1333-IRAS4A (Bottinelli et al. 2004a), NGC1333-IRAS2A (Jørgensen et al.

2005), and NGC1333-IRAS4B (Sakai et al. 2006; Bottinelli et al. 2007), which have similar chemical characteristics (Herbst & van Dishoeck 2009), with abundant saturated COMs and scarce unsaturated carbon-chain molecules.

Warm carbon-chain chemistry sources represent another class of low-mass Class 0/I protostellar sources. They are characterized by high excitation conditions, central concentration, and abundant unsaturated carbon-chain molecules such as hydrocarbons (e.g., C_nH , C_nH_2 , $n = 1, 2, \dots$), cyanopolyynes ($HC_{2n+1}N$, $n = 1, 2, \dots$) families and so on (Sakai et al. 2009). In contrast, they exhibit a relatively limited presence of saturated COMs (e.g., Sakai et al. 2008, 2009; Hirota et al. 2009). These sources are also associated with dense and lukewarm circumstellar envelopes and an enhancement of gaseous CO_2 (Sakai et al. 2009). The first confirmed WCCC source is L1527, which contains the low-mass Class 0 or I protostar IRAS 04368+2557 (Sakai et al. 2008; Ohashi et al. 1997; Sakai & Yamamoto 2013). Later observations confirm additional sources, such as IRAS 15398–3359 in Lupus and IRAS 18148–0440 in L483, as WCCC sources or candidates, which exhibit abundant carbon-chain molecules (Hirota et al. 2009; Sakai et al. 2009; Higuchi et al. 2018). These carbon-chain molecules in warm, extended, dense regions are formed through the evaporation of CH_4 ice from dust grains (Sakai et al. 2009; Sakai & Yamamoto 2013).

Distinctive chemical compositions are evident in these prototypical sources: the hot corino IRAS 16293 exhibits a dearth of carbon-chain molecules, whereas the WCCC source L1527 does not display any detectable COMs (Sakai & Yamamoto 2013). To date, two major reasons have been proposed to explain their chemical variations: different timescale of prestellar cores (Sakai et al. 2008; Sakai & Yamamoto 2013) disproved by the model of Aikawa et al. (2020), and different illumination by the UV radiation field (Spezzano et al. 2016; Kalvāns 2021). Some observations indicate that WCCC sources are found in cloud peripheries, while typical hot-corino-like sources are absent in these regions, and instead are located inside dense filamentary clouds (Lefloch et al. 2018; Higuchi et al. 2018). These observations suggest that carbon-chain molecules are more abundant in protostars with lower visual extinction of ambient clouds, which is consistent with the chemical simulations reported by Aikawa et al. (2020). Bouvier et al. (2022) found that the OMC-2/3 filament appears to have a relatively lower detection rate of hot corinos (i.e., $\sim 23\%$), in comparison with the Perseus low-mass star-forming region, where hot corinos were detected in approximately 60% of sources by the Perseus ALMA Chemistry Survey (Yang et al. 2021). Studying in detail the influence of UV photons illumination and cosmic-ray irradiation on WCCC sources, Kalvāns (2021) found that the abundances of carbon-chain molecules can be influenced by cosmic ray and UV irradiation, while the abundances of COMs have no clear correlation with radiation.

Some hybrid sources are also identified by interferometer observations (e.g., Graninger et al. 2016; Imai et al. 2016; Oya et al. 2017; Jacobsen et al. 2019; Bouvier et al. 2020), in which the emissions of carbon-chain species are from extended envelope ($r \sim$ a few $10^2 - 10^3$ AU), and emissions of COMs are centrally concentrated ($r \lesssim 100$ AU). Additionally, by analyzing the C_2H/CH_3OH ratio, Higuchi et al. (2018) discovered that most sources display intermediate chemical features between these two distinct types. There are only a few theoretical works investigating both WCCC and hot corino chemistry (e.g., Aikawa et al. 2020), but reproducing the scarce saturated COMs in canonical WCCC sources is challenging.

Dynamics is essential for studying the chemical compositions of protostellar cores. There are numerous theoretical

and numerical simulation approaches to low-mass star formation, such as the semianalytical L-P model (Larson 1969; Penston 1969), self-similar expansion wave collapse model (Shu 1977), complicated 1-dimensional radiation hydrodynamical model (Masunaga & Inutsuka 2000), 2-dimensional hydrodynamical model, and full 3-dimensional radiation magnetohydrodynamics model (Tomida et al. 2010). On the other hand, numerous works have indicated that carbon-chain molecules and COMs in the protostellar cores are mainly originated from infalling envelopes rather than rotating disks (e.g., Myers et al. 1995; Pineda et al. 2012; Imai et al. 2019; Jacobsen et al. 2019; Belloche et al. 2020). Therefore, the expansion wave collapse model can satisfy our research aims to study molecular spatial distributions, without incurring enormous computational costs as radiation hydrodynamical simulations (e.g., Aikawa et al. 2008, 2020).

This paper is organized as follows. In Sect. 2, we describe in detail physical and chemical models. To explore whether hybrid sources are a common occurrence, we reproduce the chemical characteristics of carbon-chain molecules and COMs in the fiducial model in Sect. 3. Additionally, we compare our results with some observations, including a hybrid source L483. To find out the potential reasons for chemical diversity between WCCC and hot corino sources, we explore the influence of several physical parameters on carbon-chain molecules and COMs in Sect. 4, including the visual extinction of ambient clouds, the cosmic ray ionization rate, the maximum temperature at hot corino phase, and the contraction timescale of the protostar (i.e., warm-up timescale). We discuss the reasons for the scarce COMs in the prototypical WCCC sources (e.g., L1527, IRAS16293) and potential effect of some uncertainties on simulated results in Sect. 5, followed by a brief conclusion in Sect. 6.

2. Model

2.1. Physical Model

In this paper, we adopted a 1-D spherical modified free-fall collapse (Spitzer 1978; Rawlings et al. 1992), followed by an expansion wave collapse (Shu 1977). The modified free-fall collapse, with a specific initial number density n_0 , is depicted by Rawlings et al. (1992) as follows:

$$\frac{dn}{dt} = B \left(\frac{n^4}{n_0} \right)^{1/3} \left(24\pi G m_H n_0 \left[\left(\frac{n}{n_0} \right)^{1/3} - 1 \right] \right)^{1/2}, \quad (1)$$

where t represents time, G is the gravitational constant, B is the retardation factor, and m_H is the mass of a hydrogen atom, respectively. Initially, the number density at any radius is 10^4 cm^{-3} , then the modified free-fall collapse would be truncated by a singular isothermal sphere. The density function of the singular isothermal sphere is given by Shu (1977):

$$\rho(r) = \frac{a^2}{2\pi G} r^{-2}, \quad (2)$$

where a represents the sound speed, G is the gravitational constant, and r stands for the radial distance from the core center. In most cloud cores, magnetic fields and turbulence are very weak relative to gravity (Shu et al. 1987), so we neglected their influence on the sound speed. When considering a mean molecular weight of 1.36, mainly contributed by hydrogen and helium, and assuming a constant kinetic temperature of 10 K, the sound speed is approximately 0.25 km/s. Consequently, the outer

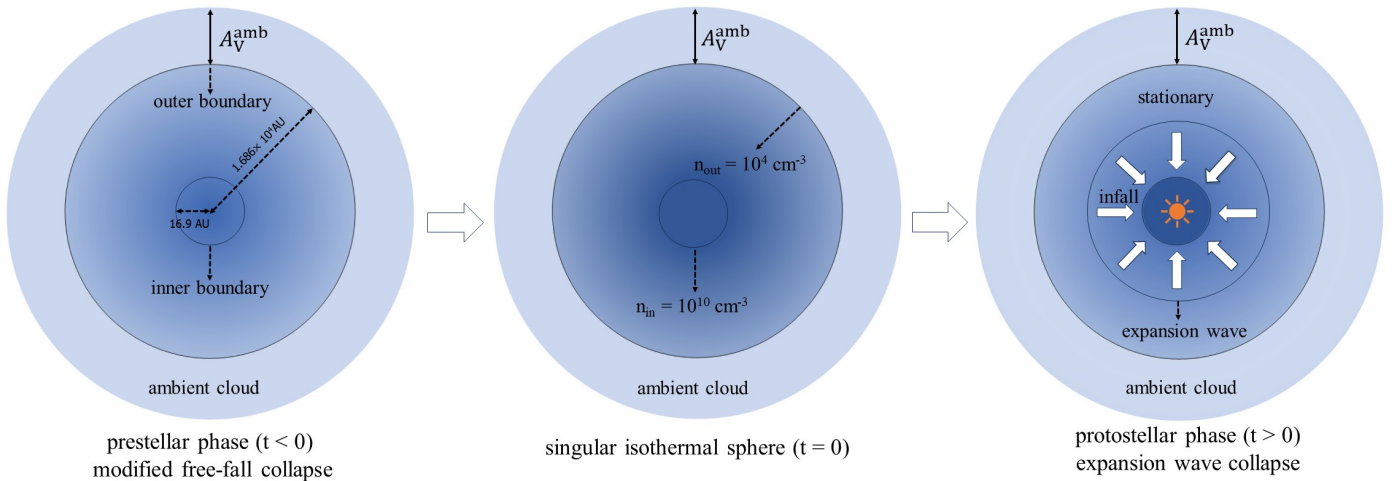


Fig. 1. Schematic view of the core model.

boundary is fixed at a radius of 1.686×10^4 AU, which corresponds to a number density of 10^4 cm^{-3} . The total mass contained within the outer boundary is about $2.3 M_{\odot}$. Given that we mainly focus on the chemical evolution in the outer envelopes, we fixed the inner boundary at ~ 16.9 AU (corresponding to a number density of 10^{10} cm^{-3}).

Our physical model consists of two main phases (Fig. 1): the prestellar phase (modified free-fall collapse) and the protostellar phase (expansion wave collapse). According to the variation of the temperature, the protostellar phase can be divided into the isothermal collapse phase, warm-up phase, and hot corino phase. Their timescales in the fiducial model are presented in Table 1. In the modified free-fall collapse, all gas parcels are stationary, but the density at any position increases with time. Once the matter density at a given radius reaches the density of the singular isothermal sphere, the density keeps constant until the density profile of the singular isothermal sphere is completed from the outside to the inside at all radii (i.e., from 16.9 to 1.686×10^4 AU). Considering the significant effects of magnetic and rotational support at the early stages, we set a moderate retardation factor B equal to 0.7. The modified free-fall collapse lasts for 7.3×10^5 yr, during which molecular abundances at the terminal stage are set to the initial molecular abundances of the expansion wave collapse.

After the singular isothermal configuration is completed, the cloud core starts to undergo an expansion wave collapse (for a detailed description, see Shu 1977). Inside the expansion wave, the matter approaches free-fall with a density distribution of $n \propto r^{-3/2}$. Outside the expansion wave, the material remains motionless at original radius, with a density distribution of $n \propto r^{-2}$. We need to follow every gas parcel that undergoes varying physical environments, and calculate the molecular abundances in a Lagrangian coordinate system. After the calculation, all parcels are transferred to Eulerian coordinates for each given time step to determine the abundance profiles of molecules with time. We assume that a gas parcel falls onto the central protostar if the radius of the parcel is less than the inner radius.

During the early stages of collapse, cooling by radiation is more efficient than heating by gravitational compression, so the core is nearly isothermal with a kinetic temperature of 10 K (Lee et al. 2004). The critical density of 10^{11} cm^{-3} has been determined by many models and observations, at which point the dust emission becomes opaque (e.g., Larson 1969). However, as the expansion wave collapse model cannot calculate the isother-

mal collapse timescale, we adopt an isothermal collapse duration of 2×10^4 yr artificially (Lee et al. 2004). When heating overtakes cooling, the temperature in the central regions begins to increase. With the gas temperature increasing, the first and second hydrostatic core (i.e., protostar) forms, respectively. Subsequently the envelopes surrounding the central protostar enter the warm-up phase, the gas and dust temperatures in the infalling envelopes are dominated by the accretion luminosity, disk luminosity, and protostellar luminosity. We consider the contraction time of a medium-mass protostar of 2×10^5 yr (Bernasconi & Maeder 1996; Viti & Williams 1999), as the warm-up timescale in the fiducial model. Afterward, the gas and dust temperatures in infalling envelopes remain constant until the end of chemical evolution (i.e., $t = 5 \times 10^5$ yr, Lee et al. 2004).

Collisions between gas and dust particles are frequent in dense regions ($> 10^4 \text{ cm}^{-3}$), so the gas temperature tends to be coupled with the dust temperature (Lee et al. 2004; Bergin & Tafalla 2007). For simplicity, we assume that the gas temperature is the same as the dust temperature in all models. In modified free-fall collapse (i.e., prestellar core), we use a fitting formula to obtain dust temperature that varies with the visual extinction and interstellar radiation fields (Hocuk et al. 2017). This formula is better suited to fit observations than other formulas (e.g., Hollenbach et al. 1991; Zucconi et al. 2001; Garrod & Pauly 2011). During the warm-up phase, we use an analytical formula to obtain the dust temperature that varies with time and radius, rather than using dust continuum radiative transfer method. This formula is given by Rowan-Robinson (1980); Viti & Williams (1999); Garrod & Herbst (2006) as:

$$T_{\text{dust}} = T_0 + (T_{\text{max}} - T_0) \left(\frac{t - t_{\text{warm}}^0}{t_c} \right)^n \left(\frac{r}{r_0} \right)^{-0.4}, \quad (3)$$

where T_{dust} is the dust temperature, T_0 is the initial temperature, 7 K (Aikawa et al. 2008; Masunaga & Inutsuka 2000), T_{max} is the maximum temperature at the end of the warm-up phase (200 K), $t_c = 2 \times 10^5$ yr is the contraction time for intermediate star formation (Bernasconi & Maeder 1996; Molinari et al. 2000; Garrod & Herbst 2006), and $n = 2$ for power-law temperature profiles (Viti et al. 2004; Garrod & Herbst 2006). After the warm-up phase, the dust temperature at any given radius remains constant until the end of chemical evolution.

At deep positions of the cloud core, cosmic rays undergo attenuation to some extent (Padovani et al. 2018), which dominates

Table 1. Fixed Various Timescales and Other Physical Parameters in the Fiducial Model

Prestellar timescale	7.3×10^5 yr
Isothermal collapse timescale	2.0×10^4 yr
Warm-up timescale/Contraction timescale	2.0×10^5 yr
Hot corino timescale	2.8×10^5 yr
Protostellar timescale	5.0×10^5 yr
Visual extinction of ambient clouds	3.0 mag
Maximum temperature	200 K
Unattenuated FUV flux	1.7 Habing
Dust-to-gas mass ratio	0.01
Dust albedo	0.6
Dust grain radius	$0.1 \mu\text{m}$
Dust material density	3.0 g cm^{-3}
Dust site density	10^{15} cm^{-2}
Chemical desorption efficiency	0.03
Ratio of surface diffusion to desorption energies	0.4
Ratio of bulk diffusion to desorption energies	0.8
Mean molecular weight	1.36

molecular chemistry relative to UV photons. Furthermore, cosmic rays significantly affect WCCC and hot corino chemistry in protostellar cores (see Sect. 4.2), so we adopted a fitting formula that varies with the total column density N_{H} , rather than treating it as a constant. This formula is given by Padovani et al. (2018) as:

$$\log_{10} \zeta = \sum_{k \geq 0} c_k \log_{10}^k N_{\text{H}}, \quad (4)$$

where c_k are coefficients of the polynomial fit (see model L in Table F.1 from Padovani et al. 2018). We assume that the cloud core is exposed to the Draine (1978) radiation field, which is equal to approximately 1.7 times the Habing (1968) local interstellar radiation field. Outside the cloud core, we adopt a high visual extinction of ambient clouds of 3.0 mag (Aikawa et al. 2020). The relation between the visual extinction A_V and the total column density of protons N_{H} is given by Bohlin et al. (1978) as $A_V = 5.34 \times 10^{-22} N_{\text{H}}$.

2.2. Chemical Model

The chemical models in this study are carried out using the astrochemical code Chempl (Du 2021), which supports the three-phase formulation of interstellar gas-grain chemistry following the approach of Hasegawa & Herbst (1993) and Garrod & Pauly (2011). In this code, species in the mantle are completely inert, and the transition of species on dust grain surfaces to mantles is achieved through the exposure and coverage (for a detailed description, see Du 2021). For the gas-phase chemistry, Du (2021) used the UMIST database for astrochemistry 2012 network (UDFA 12, McElroy et al. 2013). Their surface reactions mainly involve the formation of HCHO, CH₃OH, H₂O, H₂O₂, and a few additional reactions, which are a combination of selected reactions from some other works (e.g., Allen & Robinson 1977; Tielens & Hagen 1982; Hasegawa et al. 1992). To meet our research requirements in the hot chemistry, we have implemented several modifications as follows.

Some calculations and experiments have shown that sub-surface processes, such as photodissociation, diffusion, and recombination, can operate in interstellar grain mantles (e.g., An-

Table 2. Initial Abundances with Respect to Total Hydrogen in the Fiducial Model

Species	Abundance ¹	Species	Abundance ¹
H	3.33(-01)	Si ⁺	9.74(-09)
H ₂	3.33(-01)	Fe ⁺	2.74(-09)
He	9.00(-02)	Mg ⁺	1.09(-08)
C ⁺	7.30(-05)	Cl ⁺	1.00(-09)
N	2.14(-05)	Na ⁺	2.25(-09)
O	1.76(-04)	P ⁺	2.16(-10)
S ⁺	9.14(-08)	F	6.68(-09)

Notes. ⁽¹⁾ $A(B) = A \times 10^B$

dersson & van Dishoeck 2008; Öberg et al. 2009a). Therefore, we have made improvements to incorporate the active bulk chemistry in the three-phase model, in which bulk diffusion is driven by the diffusion of water molecules in the ice (e.g., Garrod 2013; Ruaud et al. 2016). Additionally, we set the diffusion energy in ice mantles $E_{\text{diff}}^m(i) = E_{\text{diff}}^m(\text{H}_2\text{O})$ for all the species (except H, H₂, C, N, and O) with $E_{\text{diff}}^m(i) < E_{\text{diff}}^m(\text{H}_2\text{O})$, following the treatment of Ruaud et al. 2016. The gas-phase network used in this work is based on the kinetic database for astrochemistry 2014 (KIDA 2014, Wakelam et al. 2015), and the grain network is the one presented by Ruaud et al. (2015, 2016). The grain network includes swapping reactions between species on surfaces and mantles and many reactions in mantles following Garrod (2013). Since the reaction-diffusion competition not only affects CO₂ formation on grains but also all species formed via reactions with a barrier, we use the competition mechanism for all two-body reactions in surfaces and mantles (see Ruaud et al. 2016). The Eley-Rideal and van der Waals complex-induced reaction mechanisms play an important role in the formation of some COMs (Ruaud et al. 2015), so the grain surface network in this work also includes the new surface mechanisms (van der Waals complexes and Eley-Rideal mechanisms).

Besides some reaction mechanisms, we have also made some modifications to certain reactions in the chemical network. The gas reaction rate coefficient of $\text{NH}_2 + \text{H}_2\text{CO} \rightarrow \text{NH}_2\text{CHO} + \text{H}$ was taken to be $2.6 \times 10^{-12} (T/300\text{K})^{-2.1} \exp(-26.9\text{K}/T) \text{ cm}^3 \text{ s}^{-1}$ following Barone et al. (2015)'s new insights. To treat self- and mutual- shielding, we used the analytical approach of Draine & Bertoldi (1996) for H₂, tabulated rates for CO and N₂ photodissociation (e.g., Visser et al. 2009; Li et al. 2013). Various studies on species on water ice have reported diffusion-desorption ratios from 0.3 to 0.6 (Ruffle & Herbst 2000; Karssemeijer & Cuppen 2014; Minissale et al. 2016a; He et al. 2018). We assume $E_{\text{diff}}^s = 0.4 \times E_{\text{des}}^s$ (except for H atoms; Garrod & Herbst 2006; Ruaud et al. 2016; Aikawa et al. 2020) and $E_{\text{diff}}^m = 0.8 \times E_{\text{des}}^m$ (Ruaud et al. 2016) for surface and mantle species, respectively. The diffusion barrier of H atom was adopted as 230 K, which is identical to its value in some previous work (Al-Halabi & van Dishoeck 2007; Hama et al. 2012; He et al. 2018). We used a direct measurement of binding energy for atomic oxygen on dust grain surfaces of ~ 1660 K (He et al. 2015), which differs from some previous works (Garrod & Pauly 2011).

We also modified some non-thermal desorption reactions, including cosmic-ray desorption, photodesorption, cosmic-ray-induced photodesorption, and chemical desorption reactions. We used a new cosmic-ray desorption method following Kalvāns (2018), and the cosmic-ray flux was taken to be $10^4 \text{ photons cm}^{-2} \text{ s}^{-1}$ (Shen et al. 2004). We added photodesorption and cosmic-ray-induced photodesorption processes following the ap-

proach of Kalvāns et al. (2017). For CH_4 , CO , CO_2 , CH_3OH , N_2 , NH_3 , and H_2O molecules, we adopted experimental photodesorption yields (Öberg et al. 2009c,b; Bertin et al. 2013; Martín-Doménech et al. 2015; Dupuy et al. 2017; Kalvāns 2018), while we set default photodesorption yields for other species of 10^{-4} . Reactive (chemical) desorption was also taken into account, simulating the ejection of products of exothermic surface reactions. Experiments showed that the chemical desorption efficiency for partially hydrogenated reactions is very low on water ice surfaces (Minissale et al. 2016b; Chuang et al. 2018), which is consistent with theoretical calculations through Rice-Ramsperger-Kassel (RRK) theory (Garrod et al. 2007). We adopted a generic value of 0.03 for chemical desorption efficiency for all exothermic surface reactions (Garrod et al. 2007; Kalvāns 2021). Andersson & van Dishoeck (2008) estimated that the probability of UV photons being absorbed by one ice monolayer is approximately 0.007, indicating that photodissociation reactions in the ice mantle should be taken into account. Kalvāns (2018) determined an average the solid/gas photodissociation coefficient ratio of ~ 0.3 , so we applied this value to icy mantles. For the dust grain, we assume a canonical radius of $a = 0.1 \mu\text{m}$, a material density of $\rho_d = 3 \text{ g cm}^{-3}$, an average albedo of 0.6, and a dust-to-gas mass ratio of 0.01 (e.g., Aikawa et al. 2020; Kalvāns 2021). The chemical parameters are listed in Table 1. For the initial elemental abundances in the fiducial model, we assumed the so-called low-metal values, which are identical to those in Kalvāns (2021), except for hydrogen (Garrod et al. 2008). We assumed gas-phase species were in atomic or ionized form, except for hydrogen, which was in molecular form. The initial abundances in the fiducial model are given in Table 2.

3. Results

3.1. Physical Evolution in the Fiducial Model

Several physical parameters dominate chemical processes in cloud cores, including number density, gas temperature, dust temperature, visual extinction, and cosmic-ray ionization rate. The number density, infall velocity, dust temperature, and visual extinction in the fiducial model vary with radius and time are shown in Fig. 2. Here, we define the moment of the prestellar core infall as $t = 0$. The left panels show these physical parameters as a function of time at specific gas parcels, while the right panels show the radial distributions of these physical parameters at some specific times.

During the prestellar stages (i.e., $t < 0$), the number density at each radius increases with time before reaching a value in a singular isothermal sphere (Rawlings et al. 1992). Subsequently, the number density at this position stays constant until the gas parcel begins to infall (i.e., $t = 0$). The number density in the outermost layer keeps at 10^4 cm^{-3} , while it in the innermost layer increases from 10^4 to 10^{10} cm^{-3} . Although the density at each position gradually increases, all gas parcels remain stationary. The dust temperature at different radii decreases over time due to fewer UV photons heating the dust grain with increasing visual extinction. Generally, the dust temperature keeps at approximately 10 K at any radius, being higher outwards. The visual extinction at each radius gradually increases to the corresponding maximum value in the prestellar phase, until the gas parcel begins to infall. The visual extinction in the innermost layer increases from 4.3 to 1348 mag, while the visual extinction in the outermost layer is stable at 3.0 mag.

When the inside-out collapse begins, the material in the regions swept by the expansion wave starts to infall toward the cen-

ter. Additionally, the closer to the center, the faster the material falls. In the Lagrangian coordinates (see left panels in Fig. 2), the number densities of specific gas parcels keep constants before infall occurs, then gradually increase until gas parcels fall into the central protostar (i.e., $r < r_{\text{in}} = 16.9 \text{ AU}$). However, in the Eulerian coordinates (see right panels in Fig. 2), the number density at a fixed radius remains constant, then gradually decreases after the expansion wave passes by. The material at a fixed radius falls increasingly faster over time. During the isothermal collapse phase (i.e., $t < 2 \times 10^4 \text{ yr}$), gas and dust temperatures are fixed at 7 K. When the protostellar envelope enters the warm-up phase, the temperature in the innermost layer gradually increases from the initial 7 K to 200 K and remains there. The visual extinction exhibits characteristics that vary with time and radius, which is similar to those of number densities in both Lagrangian and Eulerian coordinates.

3.2. Chemical Evolution in the Prestellar Core

Since chemical compositions in the protostellar envelope inherits from the prestellar core, we have to first investigate the molecular distribution during the prestellar phase. Panel (a-b) in Fig. 3 show the radial distribution of some canonical carbon-chain molecules detected in prototypical WCCC sources, including C_nH , C_nH_2 , HC_{2n+1}N families ($n = 1, 2, \dots$), and some precursors related to WCCC at the end of the prestellar phase. Most carbon-chain molecules are concentrated around the position of $4 \times 10^3 \text{ AU}$, implying the emission of these molecules mainly comes from the outer regions of the prestellar core. Carbon-chain molecules are rapidly adsorbed on the dust grain (adsorption timescale of $\sim 1 \text{ yr}$) due to high densities near the prestellar center, while their abundances are low near the peripheries due to strong UV photodissociation processes. The peak abundances of most of carbon-chain molecules, with the exception of CH_4 , CCH , C_2H_2 , and C_4H_2 , are lower than 10^{-9} . For instance, the peak abundances of HC_3N and HC_5N molecules are close to the observed values in high-mass star-forming starless cores ($X(\text{HC}_3\text{N}) \sim 10^{-11} - 10^{-10}$, and $X(\text{HC}_5\text{N}) \sim 10^{-12} - 10^{-11}$; Taniguchi et al. 2018). This suggests these abundant molecules observed in the protostellar core are not primarily inherited from the prestellar core, but instead another mechanism is responsible for their formation, known as the WCCC mechanism.

Panel (c-d) in Fig. 5 show the radial distributions of some saturated COMs detected in protostellar cores at the end of prestellar phase (i.e., $t = 0$). These COMs are mainly produced on dust grain surfaces by the thermal hopping or quantum diffusion of radicals in the prestellar core. For instance, the depleted CO molecule can be hydrogenated by hopping H atom, forming H_2CO and CH_3OH efficiently, which has been successfully confirmed by laboratory experiments (e.g., Watanabe et al. 2003). Similar to the distributions of carbon-chain molecules, COMs are mainly concentrated at $r \sim 10^3 - 10^4 \text{ AU}$. In high visual extinction regions ($A_V > 5 \text{ mag}$), gaseous COMs mainly decrease through adsorption processes, while those in outer layers are mainly destroyed by abundant UV photons. Except for CH_3OH molecules, the peak abundances of most COMs are lower than 10^{-9} , so COMs detected in protostellar envelopes are mainly not remnants from the prestellar core.

3.3. Chemical Evolution in the Protostellar Core

To understand whether the chemical hybrid sources are common phenomena, we investigate carbon-chain molecules and

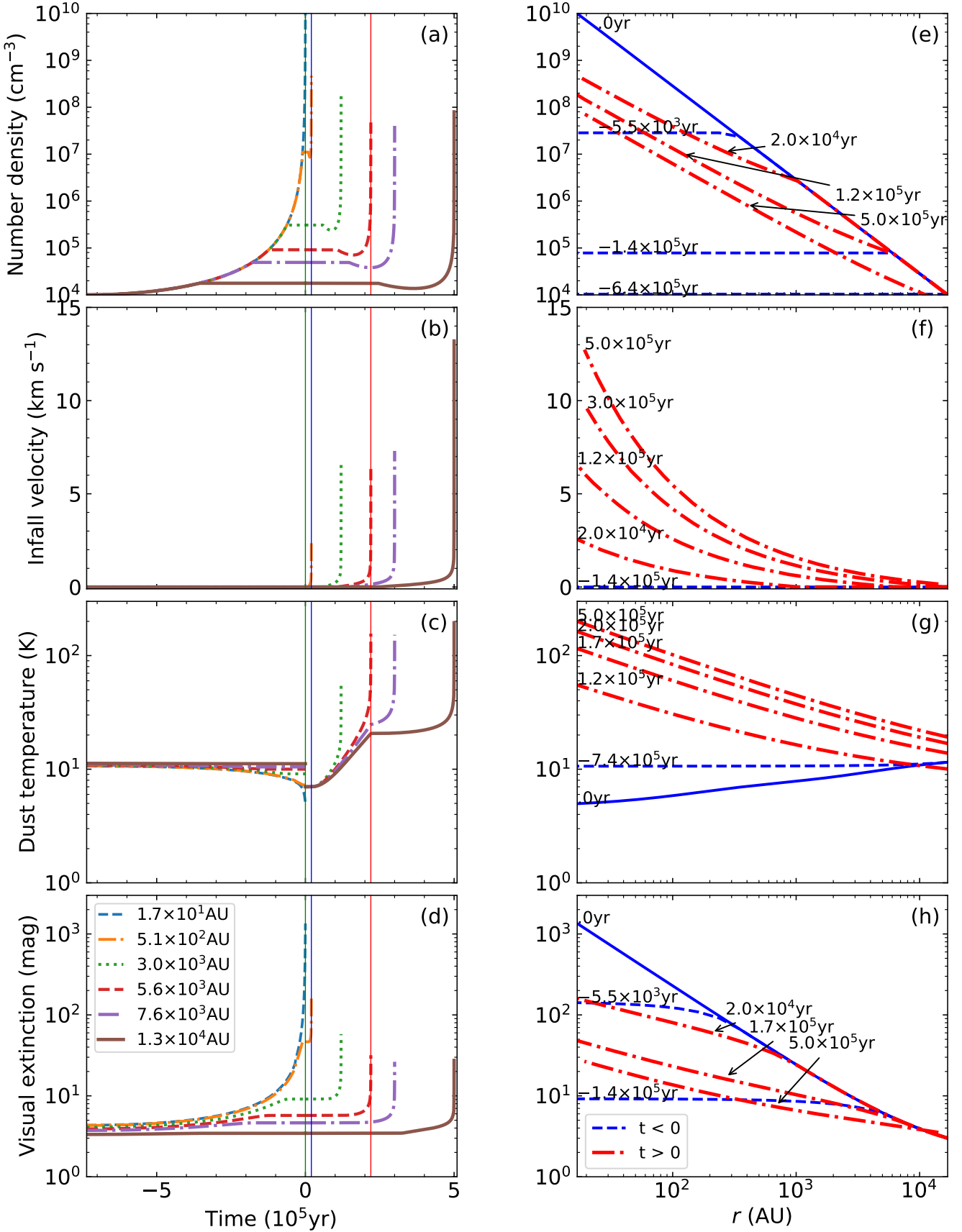


Fig. 2. Physical parameters (i.e., number density, infall velocity, dust temperature, and visual extinction) varying with time and radius in the fiducial model. (a-d) Temporal variation of these physical parameters in specific gas parcels which initially locate at $r = 16.9 \text{ AU}$, $5.1 \times 10^2 \text{ AU}$, $3.0 \times 10^3 \text{ AU}$, $5.6 \times 10^3 \text{ AU}$, $7.6 \times 10^3 \text{ AU}$, and $1.3 \times 10^4 \text{ AU}$. The three vertical lines (i.e., green, blue, and red line) indicate the initial moment of infall motion (i.e., $t = 0$), the beginning moment of warm-up (i.e., the birth of the protostar, $t = 2 \times 10^4 \text{ yr}$), and the end of warm-up phase (i.e., $t = 2.2 \times 10^5 \text{ yr}$), respectively. (e-h) Radial distributions of these physical parameters at some specific times. The times shown are relative to the initial moment of infall motion.

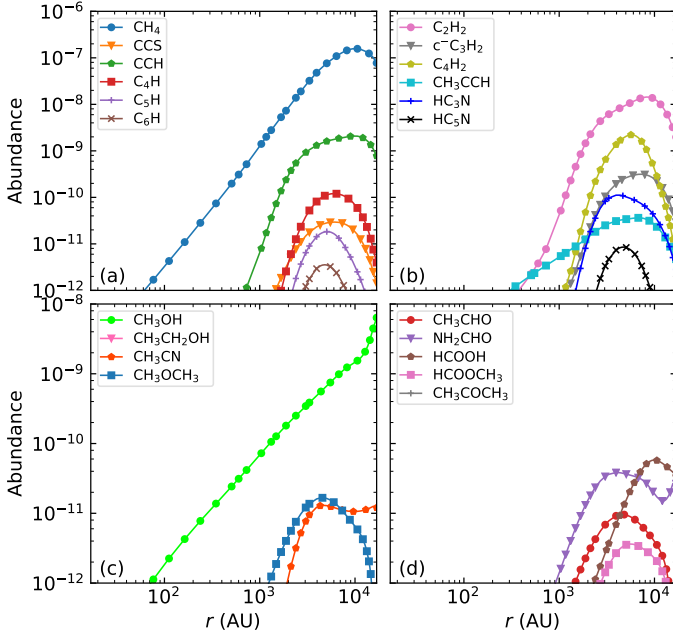


Fig. 3. Radial distributions of some gaseous carbon-chain molecules (a-b) and COMs (c-d) at the end of the modified free-fall collapse (i.e., $t = 0$) in the fiducial model.

COMs in the fiducial model during the protostellar phase. Figure 4 shows the radial distribution of unsaturated carbon-chain molecules and some molecules related to WCCC processes at some specific times. Here, four specific times (i.e., 1.7×10^5 , 2.2×10^5 , 3.0×10^5 , and 5.0×10^5 yr) represent different evolutionary stages. Specifically, the first two moments represent the warm-up phase, and the last two moments represent the hot corino stage when the dust temperature at each radius remains constant. The light gray shaded region in Fig. 4 is the hot corino region with dust temperature above 100 K, while the dark gray shaded region represents the WCCC region with dust temperature between 20–35 K (Aikawa et al. 2020; Kalvāns 2021).

Firstly, we take the moment of 2.2×10^5 yr as an example to show the common distribution features of carbon-chain molecules at four moments. There is a clear abundance jump for CH_4 molecule showed in the region within the dust temperature of ~ 25 K, corresponding to its sublimation temperature (T_{sub}). When the dust temperature is above 25 K, the solid CH_4 can quickly evaporate into the gas phase through thermal desorption. Subsequently, gaseous CH_4 molecules react with C^+ to produce C_2H_3^+ or C_2H_2^+ , which then react with e^- to produce the shortest carbon-chain molecules, C_2H_2 and C_2H . Long carbon-chain molecules are gradually produced through further reactions with C^+ , H , and e^- (for a detailed description, see Hassel et al. 2008; Sakai & Yamamoto 2013). Therefore, carbon-chain molecules in the WCCC regions (i.e., $2.1 \times 10^3 - 1.4 \times 10^4$ AU) are more abundant relative to cold regions. Abundance jump also appears for a few molecules, such as CH_3CCH ($T_{\text{sub}} \sim 80$ K), C_nH_2 group, and HC_{2n+1}N group. The abundances of carbon-chain molecules in most regions are higher than 10^{-10} , indicating the common occurrence of carbon-chain molecules in protostellar cores.

Based on the radial distribution of carbon-chain molecules, they can be mainly divided into two types as shown in Fig. 4. The C_nH family represents the first type, which is characterized by an extended distribution and a small central dip around the pro-

tostar. Numerous observations of CCH and C_4H have provided evidence for the widespread occurrence of this spatial distribution pattern (Sakai et al. 2010; Imai et al. 2016; Oya et al. 2017; Murillo et al. 2018). In hot corino regions (i.e., $r < 100$ AU), the destruction of C_nH molecules is dominated by the following reaction (the activation barrier is ~ 950 K):



which accounts for a dip structure in the intensity profile toward the protostar. The second type (including HC_{2n+1}N and C_nH_2 families) is characterized by central condensation, which is consistent with some observational evidences. For instance, $\text{c-C}_3\text{H}_2$ molecules are distributed in more shielded inner envelopes (Lindberg et al. 2017), while HC_5N exhibits very high excitation energy levels (Sakai et al. 2009; Taniguchi et al. 2023). In the lukewarm regions, HC_{2n+1}N molecules are mainly produced by the gaseous reactions (Taniguchi et al. 2019)



and



while the precursors C_{2n}H_2 are produced by the reactions



These gaseous carbon-chain molecules are accreted onto the bulk and surface of ice mantles, which occurs at $25 < T_{\text{dust}} < 100$ K. When the dust temperature approaches their sublimation temperature, they would be evaporated into the gas phase. In the hot corino regions, due to the infall timescales of gas parcels of ~ 90 yr are much less than the destruction timescales of the carbon-chain molecules, so their radial distributions show a flat structure in inner regions. Due to high activation barriers between C_nH_2 and H_2 molecules, the central dip structure as C_nH family is absent in hot corino regions.

Comparing the distributions of these carbon-chain molecules at different moments, we find some clear differences in molecular abundances. At the warm-up phase, the positions of the peak abundances for carbon-chain molecules gradually move outward, corresponding to WCCC regions. At the hot corino phase, the peak abundances of carbon-chain molecules keep at the WCCC regions (i.e., $2 \times 10^3 - 1.4 \times 10^4$ AU). As the protostellar evolution processes, the carbon-chain molecules at any radius gradually decrease, which is mainly because the CH_4 abundance near the cloud periphery is less abundant due to its rapid reaction with H_3^+ . At the late stages (e.g., $t = 5 \times 10^5$ yr), the spatial distributions of carbon-chain molecules in the protostellar envelope are strongly affected by the remnants from the prestellar core. In general, WCCC is inclined to appear during the warm-up phase, which is consistent with some models constructed by Hassel et al. (2008) and Wang et al. (2019).

Figure 5 shows the spatial distribution of saturated COMs and some molecules related to hot corino chemistry at some specific times, identical with in Fig. 4. The distribution characteristics of COMs are significantly diverse from those of carbon-chain molecules in Fig. 4, due to different formation pathways. Since COMs are mainly produced by surface reactions on dust grains, the dust temperature is the most important factor to determine their radial distributions.

Firstly, we take the time of 2.2×10^5 yr as an example to depict the similar distribution characteristics of COMs at these four moments. The abundances of COMs in hot corino regions are

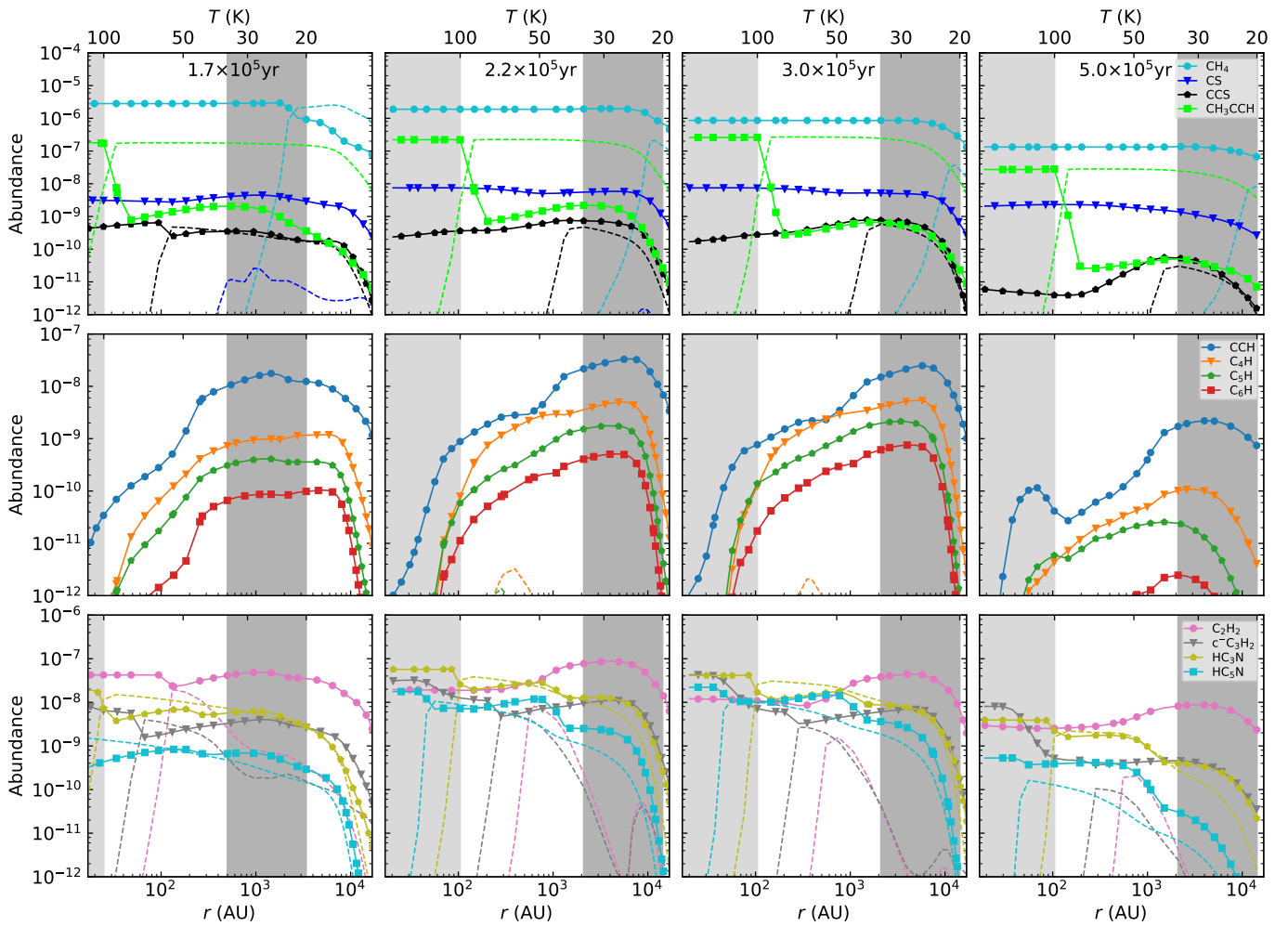


Fig. 4. Radial distribution of simple (CH_4 and CS) and carbon-chain molecules at $t = 1.7 \times 10^5$, 2.2×10^5 , 3.0×10^5 , and 5.0×10^5 yr in the fiducial model. The light gray shadow covers the hot corino regions within the dust temperature > 100 K. The dark gray shaded areas represent the WCCC regions within the dust temperature from 20 to 35 K. The different molecules are distinguished by line colors and marks. The solid lines show the gaseous abundances, while the dashed lines depict the icy abundances.

extremely higher than 10^{-10} , indicating the common occurrence of COMs in protostellar cores. Hot corino chemistry starts with the successive hydrogenation of CO molecules on the surfaces of dust grains to form CH_3OH , which serves as a fundamental COM and a precursor for more complex COMs (Öberg & Bergin 2021). In hot corino regions (i.e., $r < 100$ AU; $T_{\text{dust}} > 100$ K), most saturated COMs in ice mantles are evaporated into the gas phase by the thermal desorption. Infall timescales of gas parcels through hot corino regions (~ 90 yr) are less than destruction timescales of COMs (e.g., $t_{\text{des}} \sim 5 \times 10^5$ yr for CH_3OH), so most COMs exhibit a flat profile. Additionally, saturated COMs are mainly distributed in the regions within 100 AU near the central protostar, which is consistent with a few observations toward protostars. For example, some observations toward some hybrid sources, such as B335, L483 (Imai et al. 2016; Oya et al. 2017; Bouvier et al. 2020) showed narrow spatial distributions for saturated COMs. An abundance jump has been observed for CH_3OH and H_2CO in several low-mass protostellar sources (e.g., Maret et al. 2005; Kristensen et al. 2010), as shown in the fiducial model.

There are some clear variations in molecular abundances at these four times. During the warm-up phase, the peak abun-

dances of COMs gradually increase with time due to the expanding hot corino regions, where most COMs in ice mantles are evaporated into gas-phase. When the infall timescales are larger than the evaporation timescales of COMs, the molecular abundance can form a rapidly rising profile at $t = 1.7 \times 10^5$ yr, without generating a flat feature in inner regions as at other moments in Fig. 5. At the late stages, the material near the outer boundary of protostellar envelope begins to infall towards the protostar. The COMs and their precursors at the periphery are rapidly destroyed by UV photons and secondary photons (destruction timescale is 1×10^4 yr for CH_3OH), leading to low abundances of COMs (i.e., $\leq 10^{-9}$) in gas phase and ice mantles.

The chemical survey toward young stellar objects in the Perseus molecular cloud complex indicates that the hybrid sources could be a widespread occurrence. Additionally, infrared observations by Graninger et al. (2016) also suggest an indispensable evidence for the hybrid sources, by observing simultaneously presence of CH_4 and CH_3OH ices. The emission of carbon-chain molecules is more extended compared to that of COMs in the protostellar core, as demonstrated in hybrid sources (Oya et al. 2017; Taniguchi et al. 2021b). The fiducial model predicts abundant saturated COMs near the innermost protostellar

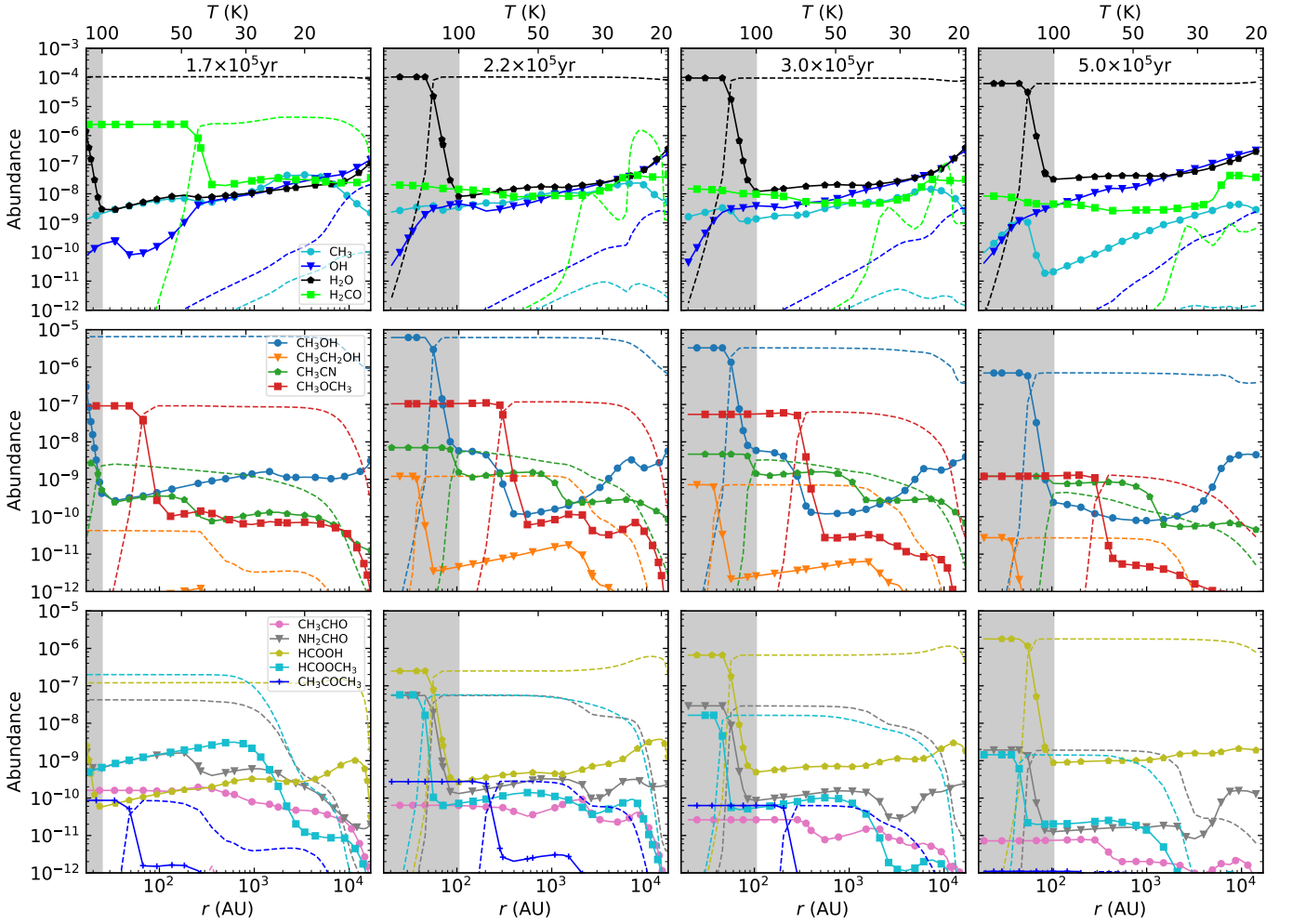


Fig. 5. Radial distribution of simple molecules (CH_3 , OH , H_2O , and H_2CO) and COMs at $t = 1.7 \times 10^5$, 2.2×10^5 , 3.0×10^5 , and 5.0×10^5 yr in the protostellar core, as in Fig. 4.

envelopes at 2.2×10^5 yr, corresponding to hot corino chemistry. Simultaneously, the model also predicts abundant unsaturated carbon-chain molecules in WCCC regions due to the sublimation of methane. Therefore, unsaturated carbon-chain molecules and saturated COMs can coexist, which has been observed in some protostellar cores (e.g., B335, Imai et al. 2016, 2019; L483, Oya et al. 2017; Jacobsen et al. 2019; Agúndez et al. 2019). Since the emissions of carbon-chain molecules and COMs are spatially separated in Figs. 4 and 5, there is no clear statistical correlation between their column densities in large sample observations (e.g., Lindberg et al. 2016).

3.4. Comparison with Observations

Generally, the $\text{CH}_4/\text{H}_2\text{O}$ abundance in bulk ice around low-mass young stellar objects (YSOs) are nearly constant within a narrow range (2–8%), basing on the ‘Cores to Disks’ Spitzer Spectroscopic Survey conducted by Öberg et al. (2008). At early warm-up phase (e.g., $t \sim 1.7 \times 10^5$ yr), the peak abundance of solid CH_4 and solid H_2O is close to 3×10^{-6} and 1×10^{-4} , respectively, so their ratio equals to 3% aligning with observed values. At hot corino stages (e.g., 3.0×10^5 yr, see in Fig. 4), most CH_4 ice evaporates into the gas phase, which may explain why approx-

imately half of low-mass YSOs lack a solid CH_4 signal (Öberg et al. 2008).

The abundances of carbon-chain molecules and COMs in the fiducial model differ from the results in some works such as Aikawa et al. (2008, 2020). The variation between our three-phase model and the two-phase or multilayered ice mantle model used in their works is one source for the differences. However, other factors may amplify chemical differences as well, such as the physical model (inside-out collapse model vs radiation hydrodynamic model). For instance, the peak abundance of NH_2CHO in the fiducial model is significantly higher, by more than one order of magnitude, compared with the simulated value in Aikawa et al. (2020). On the other hand, we did not consider several dynamical changes, such as the molecular outflow and disk formation, so our models may contradict some observed results dominated by above processes. For instance, Sakai et al. (2006) detected COMs even at a very early stage in protostellar evolution toward the low-mass protostar NGC 1333 IRAS 4B.

Among the hybrid sources identified through interferometer observations, the low-mass protostellar source L483 stands out as a representative example. It is located at a distance of 200 pc, as reported in studies such as Dame & Thaddeus (1985) and Jørgensen et al. (2002). Previously, L483 was categorized as a WCCC source due to its bright emission from carbon-

Table 3. Observed and Simulated Abundances in L483

Species	Observations ¹	Simulations ^{1,2}
CN	5.51(-09) ^a	4.13(-08)
CS	2.89(-09) ^a	8.20(-09)
SO	5.00(-09) ^a	6.44(-09)
SiO	6.50(-12) ^a	3.71(-10)
HCN	2.97(-09) ^a	7.29(-08)
HNC	5.95(-09) ^a	3.13(-08)
HCO ⁺	7.53(-09) ^a	1.29(-08)
CCH	1.28(-08) ^a	3.95(-08)
CCS	1.22(-10) ^a	6.53(-10)
HNCO	1.77(-09) ^b	6.05(-08)
c-C ₃ H ₂	5.25(-09) ^a	1.11(-08)
CH ₃ OH	7.31(-09) ^a	9.66(-09)
CH ₃ CHO	3.60(-10) ^b	2.81(-10)
HCOOCH ₃	1.07(-08) ^b	8.03(-09)
SO ₂	5.88(-03) ^c	4.43(-04)
H ₂ CS	1.18(-03) ^c	8.20(-03)
HC ₃ N	2.94(-02) ^c	1.45(-02)
NH ₂ CHO	5.88(-04) ^c	1.30(-02)
CH ₃ OCH ₃	4.71(-03) ^c	3.79(-02)
CH ₃ CH ₂ OH	5.88(-03) ^c	4.70(-05)

Notes. ⁽¹⁾ $A(B) = A \times 10^B$. ^(a) The fractional abundance relative to H₂ is from Agúndez et al. (2019), and the spatial resolution is ~ 5000 AU. ^(b) The fractional abundance relative to H₂ is from Oya et al. (2017), and the spatial resolution is ~ 100 AU. ^(c) The fractional abundance relative to CH₃OH is from Jacobsen et al. (2019), and the spatial resolution is ~ 20 AU. ⁽²⁾ The simulated beam-average fractional abundances have already been smoothed to their respective spatial resolutions. Boldface indicates a disagreement of more than one order of magnitude between the observed and modeled value.

chain molecules such as HC₃N (e.g., Hirota et al. 2009). However, high-resolution observations recently revealed an active hot corino chemistry near the protostar (e.g., Oya et al. 2017; Jacobsen et al. 2019). Meanwhile, it exhibits an exceedingly rich chemical composition, including several new identified interstellar molecules such as HCCO (Agúndez et al. 2015b), NCCNH⁺ (Agúndez et al. 2015a), NCO (Marcelino et al. 2018a), etc. Based on above considerations, we selected Class 0 object L483 as a reference for comparison with the fiducial model. These molecules used for comparison are listed in Table 3, with references from Oya et al. (2017); Agúndez et al. (2019); Jacobsen et al. (2019). The angular resolutions in these articles are 0.5'', 25'', and 0.1'', corresponding to spatial resolutions of 100, 5000, and 20 AU, respectively. For molecules involved in multiply works, we adopted their observed values according to the fitting goodness. In Agúndez et al. (2019)'s work, we selected molecules with line widths higher than 1.0 km/s, which is mainly because molecules with low line widths primarily originate from its cold ambient cloud, rather than from warm or hot compact regions.

In the case of low spatial resolution, the abundances of centrally concentrated molecules can be severely diluted, so we need to calculate average column densities of these molecules. To assess the column densities of molecules at each position along the line-of-sight, we used spherical protostellar envelopes. Subsequently, by smoothing the column density at each position for different telescopes, we obtained the average column densities and fractional abundances for listed molecules in Table 3. One method to quantify the overall goodness between simulations and observations is the "mean confidence level" (Garrod et al. 2007; Hassel et al. 2008). The confidence level of specie i , des-

ignated by κ_i , indicates the level of agreement between simulated values X_i and observed values X_i^{obs} , thus:

$$\kappa_i = 1 - \text{erf}\left(\frac{|\log(X_i) - \log(X_i^{\text{obs}})|}{\sqrt{2}\sigma}\right) \quad (9)$$

where erf is the error function, and σ is the standard deviation. We adopted quantitative standard of one order of magnitude between the observed and simulated values. Therefore, the mean confidence level κ is 0.317, when $\sigma = 1$. We got the maximum κ of 0.508, with the best-fitting time being 1.965×10^5 yr.

Another method to assess the global agreement is the fitting number, which represents the species that align with the observations within one order of magnitude. At the fitting time, out of the 20 molecules analyzed, 14 exhibited successful fitting. However, there were six molecules (SiO, SO₂, HCN, HNCO, NH₂CHO and CH₃CH₂OH) that did not fit well. If we consider only unsaturated carbon-chain molecules and saturated COMs, 8 out of 10 molecules can be fitted well. Overall, the fiducial model can reproduce canonical characteristics of WCCC and hot corino chemistry in hybrid source L483.

4. Possible reasons for chemical differences between WCCC and hot corino sources

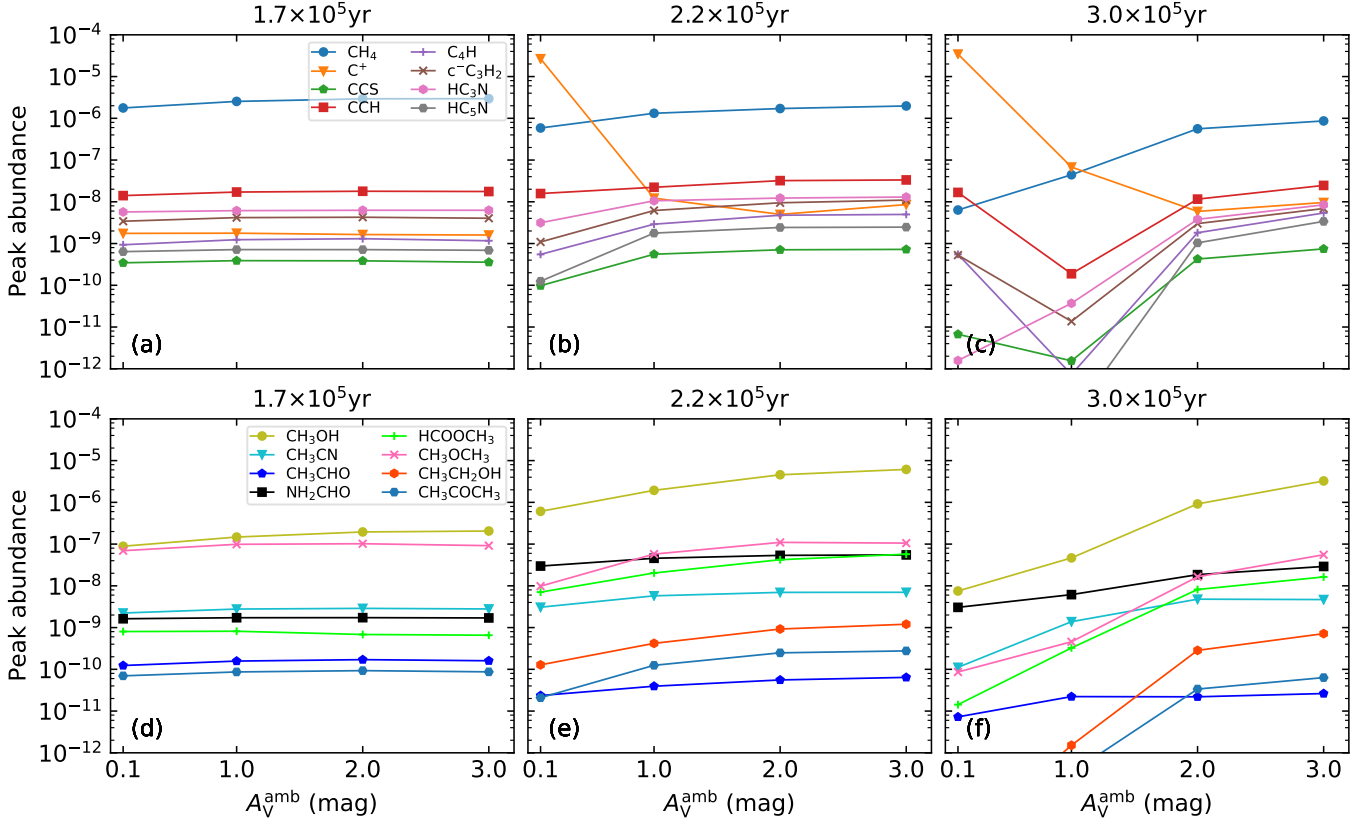
To figure out main factors leading to chemical differences between WCCC sources and hot corino sources, we investigate the dependence of carbon-chain molecules and COMs on several physical parameters. We adopt different values of the visual extinction of ambient clouds ($A_V^{\text{amb}} = 0.1, 1, 2, 3$), cosmic-ray ionization rate ($\zeta = 3 \times 10^{-18}, 3 \times 10^{-17}, 3 \times 10^{-16} \text{ s}^{-1}$; Neufeld et al. 2010; Indriolo et al. 2010; Indriolo & McCall 2012; Neufeld & Wolfire 2017), the maximum temperature ($T_{\text{max}} = 150, 200, 250, 300 \text{ K}$), and the contraction timescale ($t_c = 7 \times 10^4, 2 \times 10^5, 5 \times 10^5$ yr; Bernasconi & Maeder 1996). The values of the varied physical parameters are listed in Table 4. The abundances of most unsaturated carbon-chain molecules and saturated COMs at late stage (i.e., 5×10^5 yr) are lower than 10^{-9} , as shown in Figs. 4 and 5, showing weak WCCC and hot corino chemistry. Therefore, we no longer consider the dependence of WCCC and hot corino chemistry on these physical parameters at $t = 5 \times 10^5$ yr.

4.1. Dependence on Visual Extinction of Ambient Clouds

Numerous observations have indicated that interstellar radiation field and visual extinction of ambient clouds can drive the chemical differences among protostellar cores. Spezzano et al. (2016) found that chemical variation can be influenced by different intensity of radiation from interstellar fields, as observed in the L1544 prestellar core. Their findings revealed that photochemistry can maintain more C atoms in the gas phase, facilitating the carbon-chain production. Another study from Sicilia-Aguilar et al. (2019) indicated IC 1396A is resembled with the hybrid sources in chemical features, in which WCCC was attributed to the UV irradiation. Some statistical observations suggested that WCCC sources are located at the cloud peripheries, while hot corino sources tend to be deeply embedded into dense filamentary clouds (e.g., Higuchi et al. 2018; Lefloch et al. 2018). Recently, Bouvier et al. (2022) conducted statistical observations toward the OMC-2/3 filament, and found that the detection rate of hot corinos appears to be scarce compared to Perseus low-mass star-forming regions. In general, the interstellar radiation field plays a significant role in chemical differences among the

Table 4. Varied Physical Parameters in All Models

Visual extinction of ambient clouds (A_V^{amb})	0.1, 1, 2, 3 (mag)
Cosmic-ray ionization rate (ζ)	3×10^{-18} , 3×10^{-17} , 3×10^{-16} (s^{-1})
Maximum temperature (T_{max})	150, 200, 250, 300 (K)
Contraction timescale (t_{cont})	7×10^4 , 2×10^5 , 5×10^5 (yr)

**Fig. 6.** Peak abundances at specific regions vary with visual extinction of ambient clouds at some specific times. (a-c) Peak abundances of gaseous carbon-chain molecules around the CH_4 sublimation regions ($T = 20 - 35$ K). (d-f) Peak abundances of gaseous COMs around the hot corino regions ($T \geq 100$ K).

low-mass protostars. Here we take the visual extinction of ambient clouds as an example, to explore the influence of the interstellar fields.

Figure 6 shows peak abundances of gaseous carbon-chain molecules around the CH_4 sublimation regions (i.e., WCCC regions within the dust temperature from 20 to 35 K) and gaseous COMs around the hot corino regions (i.e., the dust temperature of ≥ 100 K) varying with the visual extinction of ambient clouds (A_V^{amb}) at some specific moments. Carbon-chain molecules primarily are formed in the gas phase, as shown in Fig. 4, so the peak abundances of carbon-chain molecules at any time are not significantly affected by non-thermal desorption mechanisms (e.g., cosmic-ray desorption, photodesorption, and chemical desorption). Since A_V^{amb} mainly affects chemical results by photodissociation reactions, which are not the major destruction pathways in inner regions, the peak abundances of carbon-chain molecules are insensitive to this factor at early warm-up stages (e.g., $t = 1.7 \times 10^5$ yr). At the time of 2.2×10^5 yr, the peak abundances of carbon-chain molecules slightly grow with increasing A_V^{amb} , due to weak photodissociation processes. At hot corino phase ($t > 2.2 \times 10^5$ yr), the peak abundances of carbon-chain

molecules reach to the minimum value of $< 10^{-9}$ at $A_V^{\text{amb}} \sim 1.0$ mag. At lower A_V^{amb} , strong UV photons quickly dissociate CO molecules, generating more C atoms and C^+ ions, which accelerates the formation of carbon-chain molecules through the WCCC mechanism mentioned in Sect. 3.3. This explains some observations that the $\text{c-C}_3\text{H}_2$ emission is effectively enhanced due to the UV radiation from a Herbig Be star (Taniguchi et al. 2021a), and that WCCC sources tend to be located at the cloud boundaries (e.g., Higuchi et al. 2018; Lefloch et al. 2018). At $A_V^{\text{amb}} \geq 2.0$ mag, the production of C^+ ions primarily depends on secondary photons generated by cosmic rays due to the strong CO self-shielding, so the C^+ abundance remains at a low level. Meanwhile, the destruction of CH_4 and carbon-chain molecules is ineffective by photodissociation reactions, so their peak abundances slightly increase with increasing A_V^{amb} .

In contrast, COMs are mainly evaporated into the gas phase through the thermal desorption, as shown in Fig. 5, so their peak abundances are not effectively affected by non-thermal desorption mechanisms. At warm-up phase ($t = 2 \times 10^4 - 2.2 \times 10^5$ yr), the peak abundances of COMs slightly grow with increasing A_V^{amb} , due to slow photodestruction rates. At hot corino phase,

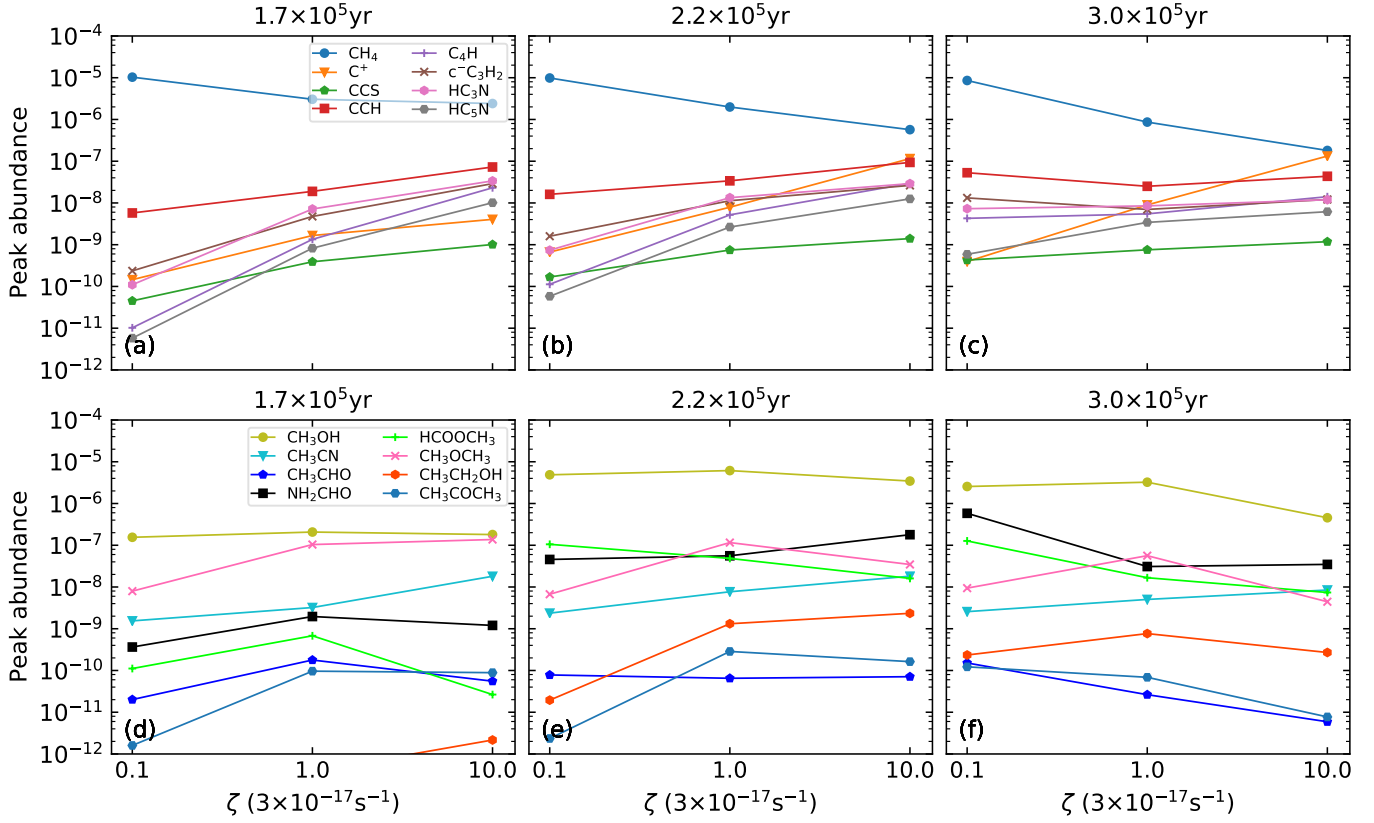


Fig. 7. Peak abundances at specific regions vary with cosmic ray ionization rates at some specific times. (a-c) Peak abundances of gaseous carbon-chain molecules around the CH_4 sublimation regions. (d-f) Peak abundances of gaseous COMs around the hot corino regions.

COMs in hot corino regions are formed on the dust surfaces and subsequently evaporated into the gas phase through thermal desorption processes. At a high A_V^{amb} , less UV photons weaken the photodissociation of COMs and their precursors, producing high peak abundances, which is consistent with high detection rate of hot corino sources in Perseus low-mass star-forming regions (Yang et al. 2021) compared to in the OMC-2/3 filament reported by Bouvier et al. (2022). As A_V^{amb} increases from 0.1 to 3.0 mag, the peak abundances of most COMs increase by about two orders of magnitude. This explains statistical observations indicating that hot corino sources are predominantly located in inner regions (e.g., Higuchi et al. 2018; Lefloch et al. 2018). Overall, the variation of A_V^{amb} can lead to the chemical differences between WCCC sources and hot corino sources.

4.2. Dependence on Cosmic Rays Irradiation

The cosmic ray ionization rate is another important physical parameter that can influence the chemical differences among low-mass protostars. Kalvāns (2021) found that the WCCC features in protostellar cores may originate from regions irradiated by cosmic rays, while the abundances of COMs have no clear correlation with radiation. They utilized UDFA 12 network launched by McElroy et al. (2013), which differs from the KIDA 2014 network. The potential impact of differences between these two networks on our simulated results is discussed in Sect. 5.2. On the other hand, they employed a single-point physical model that cannot accurately calculate the peak abundances observed in the hot corino regions. Therefore, we reinvestigate the impact of cosmic ray ionization rates on peak abundances of carbon-chain molecules and COMs.

Figure 7 shows the peak abundances of gaseous carbon-chain molecules and COMs varying the cosmic ray ionization rates at some specific times. Since the peak abundances of carbon-chain molecules and COMs are affected differently by cosmic ray ionization rates, we analyze their responses to this physical parameter separately. The peak abundances of carbon-chain molecules show a significant increase with enhancing cosmic rays, except for the reduced precursor molecule - CH_4 . As the cosmic ray ionization rate increases, the dissociation of CO and CH_4 molecules accelerates, producing more C atoms. Subsequently, C atoms are ionized into C^+ by the cosmic-ray-induced photoreactions and react with CH_4 molecules through the WCCC mechanism, leading to more abundant unsaturated carbon-chain molecules and lower peak abundances of CH_4 . At $\zeta = 3 \times 10^{-16} \text{ s}^{-1}$, the peak abundances of most carbon-chain molecules are higher than 10^{-9} , indicating that cosmic rays contribute to WCCC processes.

The influence of cosmic ray ionization rate on the peak abundances of COMs is relatively complex. This is mainly because COMs and their precursors are affected by various reaction types, such as cosmic ray desorption, cosmic-ray-induced photodesorption, cosmic-ray-induced photodissociation in gas phase and ice mantle, and cosmic-ray reactions. Additionally, the formation pathways of COMs vary significantly, so we cannot give a conclusion regarding to the impact of cosmic rays on the peak abundances of COMs. One can study how the peak abundance of a specific molecule vary with the cosmic ray ionization rate, by analyzing its main formation and destruction reactions in the chemical network. The variation of the cosmic ray ionization rate can lead to differences in WCCC, but the response of hot corino chemistry to its variation is highly dependent on the species.

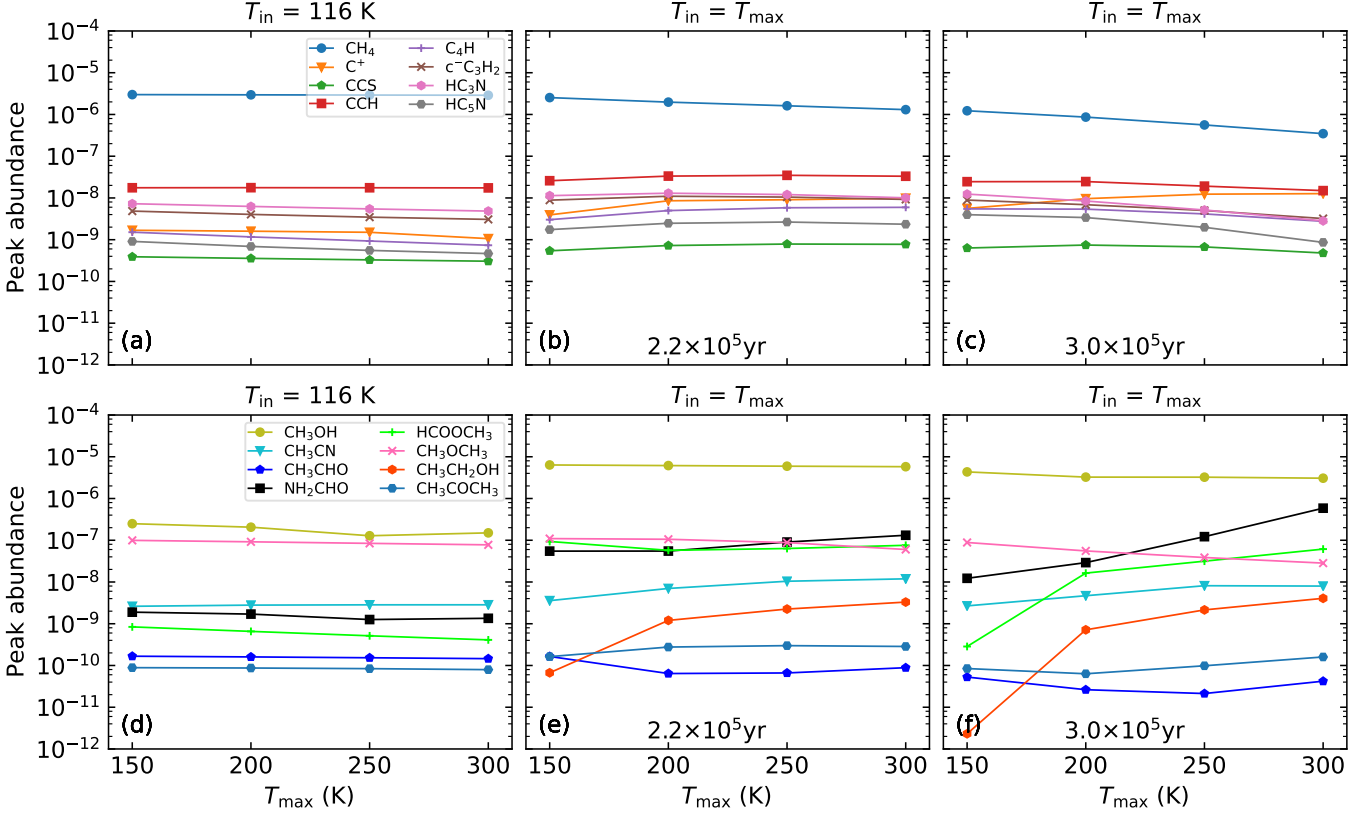


Fig. 8. Peak abundances at specific regions vary with the maximum temperature at some fixed temperatures in the innermost layer or times. (a-c) Peak abundances of gaseous carbon-chain molecules around the CH_4 sublimation regions. (d-f) Peak abundances of gaseous COMs around the hot corino regions.

4.3. Independence on Maximum Temperatures in Hot Corinos

We explored how some physical parameters at warm-up phase of the protostar as well, such as the maximum temperature and contraction timescale, influence WCCC and the hot corino chemistry. Some observations indicated that the abundance and detection number of COMs statistically do not have a direct relation with protostellar properties such as L_{bol} and T_{bol} (e.g., Higuchi et al. 2018; Yang et al. 2021), implying that the protostellar properties may not lead to differences in COMs among protostars. On the other hand, the luminosity of prototypical WCCC sources (e.g., $1.9 L_{\odot}$ in L1527; $1.8 L_{\odot}$ for IRAS 15398) tends to lower than that of prototypical hot corino sources, for instance, $9.1 L_{\odot}$ in NGC 1333 IRAS4A and $22 L_{\odot}$ in IRAS 16293 (Froeblich 2005; Crimier et al. 2010; Kristensen et al. 2012; Jørgensen et al. 2013; Karska et al. 2013). This suggests that the chemical differentiations between hot corino sources and WCCC sources may be influenced by the protostellar luminosity, which affects some physical parameters at warm-up phase such as maximum temperature.

Considering above observed results, we attempt to investigate the influence of the maximum temperature at warm-up phase (T_{max}) on the peak abundances of carbon-chain molecules and COMs, as shown in Fig. 8. Note that the peak abundances of carbon-chain molecules and COMs are compared at the same temperature in the innermost layer (T_{in}) at the first moment, while they are compared at the same times at hot corino stages (i.e., $t \geq 2.2 \times 10^5$ yr), as shown in Fig. 6. At warm-up moments, the time to reach the same T_{in} differs for different T_{max} , so one expects variations in the simulated results. At warm-up and hot

corino stages, the peak abundances of carbon-chain molecules are insensitive to T_{max} . Even at a high temperature, HC_{2n+1}N families remain abundant, which are consistent with radio observations toward some high-mass YSOs conducted by Taniguchi et al. (2019).

COMs can be categorized into two groups based on the variations in their peak abundances with T_{max} . The peak abundances in the first group (e.g., NH_2CHO) increase with increasing T_{max} , while they in the second group (e.g., CH_3OH) decrease. The temperature in the regions where they are effectively formed in the dust surfaces is relatively high (e.g., 25 - 40 K for NH_2CHO in Fig. 5) in the first group, while it is relatively low (e.g., ≤ 25 K for CH_3OH in Fig. 5) in the second group. For COMs in the first group, the effective regions where COMs can be efficiently formed move outward, as T_{max} increases. Since the infall velocity of the gas parcels is lower in the outer layers compared to in the inner layers, the gas parcels can stay for a longer time in the effective regions at high maximum temperature, producing more solid COMs. Subsequently, the solid COMs are evaporated into the gas phase through thermal desorption reactions. For the second group of COMs, the outer boundary of their effective regions (≤ 20 K) where they are effectively formed on the dust surfaces beyond the outer boundary in this physical model (i.e., $r_{\text{out}} = 1.686 \times 10^4$ AU). Therefore, the effective regions gradually narrow with increasing T_{max} , resulting in a short time for dust surface reactions and low abundances of COMs in ice mantles. Due to the varying dependencies of peak abundances of different COMs on T_{max} , the relation between the luminosity of the protostar and the abundance of COMs as well as the kind of species is difficult to find (e.g., Higuchi et al. 2018; Yang et al. 2021).

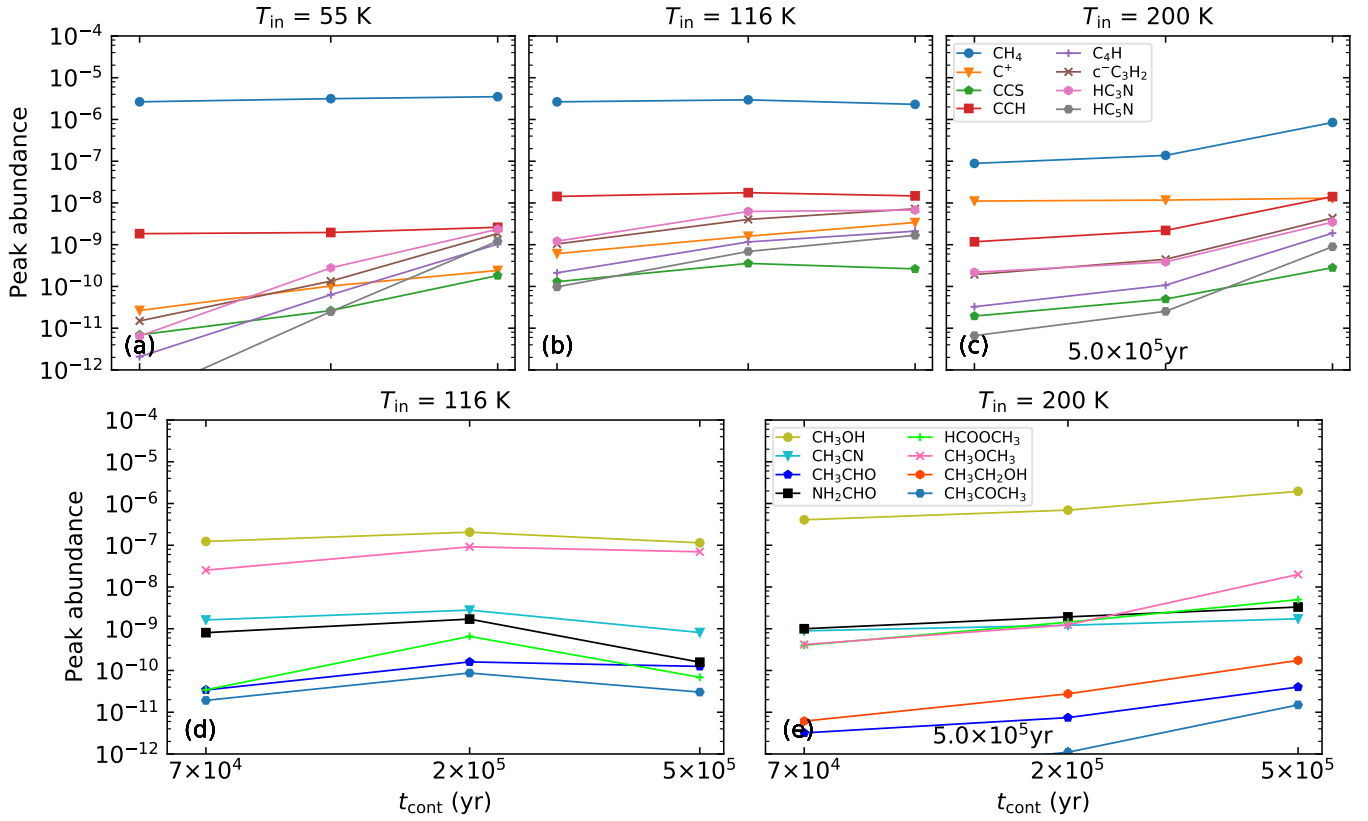


Fig. 9. Peak abundances at specific regions vary with the contraction timescale at some fixed temperatures in the innermost layer. (a-c) Peak abundances of gaseous carbon-chain molecules around the CH_4 sublimation regions. (d-e) Peak abundances of gaseous COMs around the hot corino regions.

Overall, the variation of T_{max} cannot explain the chemical differences of WCCC sources and hot corino sources.

4.4. Dependence on Contraction Timescale

The contraction timescale (t_{cont}) is an important physical parameter correlated to the protostellar mass to some extent (e.g., Bernasconi & Maeder 1996), so we investigated the influence of t_{cont} on WCCC and hot corino chemistry. Figure 9 shows the variation in peak abundances of carbon-chain molecules and COMs as a function of t_{cont} at some fixed values of T_{in} . At the larger t_{cont} , it takes longer warm-up duration to reach the same temperature. At the warm-up phase (e.g., $T_{\text{in}} = 55$ K), the duration of the WCCC processes is prolonged with increasing t_{cont} , so more carbon-chain molecules are produced. However, if the duration is too long, the carbon-chain molecules gradually be consumed by some destruction reactions in the gas phase, as shown in the central temperature of 116 K. At the final stage, the duration that the gas parcels stays in the WCCC regions where carbon-chain molecules are effectively generated is longer with a higher t_{cont} , producing more abundant carbon-chain molecules. A low t_{cont} for the high-mass protostar leads to scarce radical type carbon-chain molecules (e.g., CCH and CCS), which is consistent with some observations toward massive protostars (e.g., Taniguchi et al. 2023). At $t_{\text{cont}} = 5 \times 10^5$ yr, the abundances of most carbon-chain molecules are higher than 10^{-9} at any moment. The peak abundances of COMs vary with t_{cont} in a similar feature as carbon-chain molecules. A long contraction timescale allows solid radical molecules to stay a long duration on the dust grains, leading to high peak abundances of COMs in ice mantles

and gas phase. Overall, the variation of t_{cont} can lead to chemical differences between WCCC sources and hot corino sources.

5. Discussion

5.1. Explanation for the scarcity of COMs in prototypical WCCC sources

The relationship between the abundances of carbon-chain molecules and COMs is intricate, as demonstrated by studies conducted by Lindberg et al. (2016) and Higuchi et al. (2018). However, prototypical WCCC sources exhibit a clear chemical feature of abundant carbon-chain molecules and scarce COMs, such as L1527 and IRAS 15398, which is hard to reproduce this feature by chemical simulations (e.g., Aikawa et al. 2020). Hence we attempt to answer this question. The chemical structures are heavily depend on temperature profiles within a few hundred AU, as shown in Figs. 4 and 5. When the dust temperature is lower than the evaporation temperature of specific COMs, their abundances can maintain at a low level (can see Fig. 5). If the dust temperature in the innermost regions exceeds ~ 30 K but remains below ~ 100 K, unsaturated carbon-chain molecules may be abundant while COMs are scarce, indicating the presence of prototypical WCCC characteristics. This assumption may correspond to following two cases: the sublimation regions of COMs are apparently smaller than the beam size, or located within the rotationally supported disk (Aikawa et al. 2020). In the former scenario, the emissions of COMs can be difficult to detect due to the severe beam dilution under an insufficient spatial resolution. In the latter scenario, the spatial distribution of gaseous COMs is determined by the destruction timescale

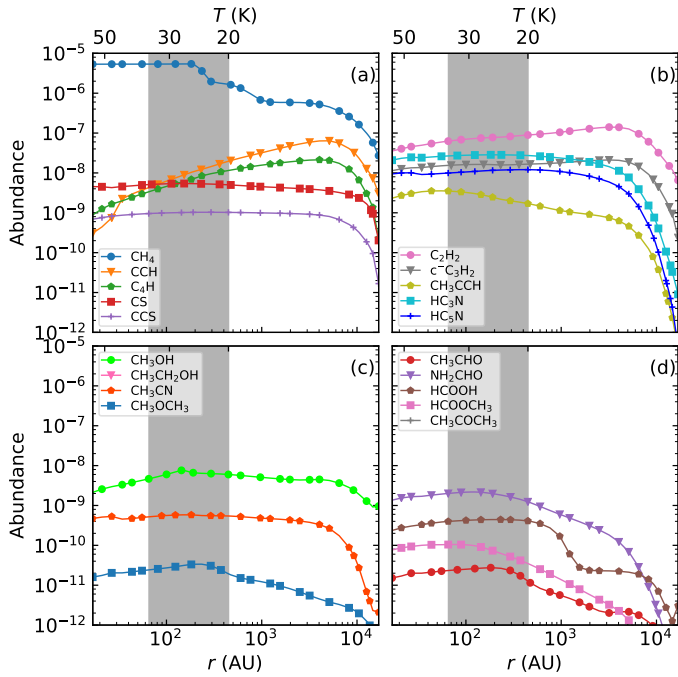


Fig. 10. Radial distribution of gaseous carbon-chain molecules (a-b) and COMs (c-d) at $t = 2.7 \times 10^5$ yr in the case of $\zeta = 3 \times 10^{-16} \text{ s}^{-1}$ and $t_{\text{cont}} = 5 \times 10^5$ yr. The dark gray shaded areas represent the WCCC regions ($T_{\text{dust}} = 20 - 35$ K).

and the radial migration timescale of gas parcels within the disk. If the migration timescale is much larger than the destruction timescale of COMs, the emissions of COMs in the disk are still difficult to detect due to low abundances.

Considering the influence of cosmic rays and the contraction timescale of the protostar on WCCC and hot corino chemistry in Sect. 4, we adopted a high cosmic-ray ionization rate of $3 \times 10^{-16} \text{ s}^{-1}$ and a long contraction timescale of 5×10^5 yr as an example to reproduce more abundant carbon-chain molecules and scarce COMs in prototypical WCCC sources. Figure 10 shows the radial distribution of carbon-chain molecules and COMs at the moment of 2.7×10^5 yr in this case, when the innermost temperature is only ~ 55 K. The ice CH_4 molecules are evaporated into the gas phase in WCCC regions through the thermal desorption mechanism, leading to a high abundance of gaseous CH_4 of 4×10^{-6} , which activates WCCC even in the vicinity of the protostar (i.e., $r \sim 100$ AU). The abundances of long carbon-chain molecules are mostly above 10^{-9} in WCCC regions, while C_nH_2 and HC_{2n+1}N groups are also abundant in the compact regions. Therefore, the protostar consists of a WCCC core, rich in small molecules, such as $\text{c-C}_3\text{H}_2$, and an extended envelope, rich in CCH and C_4H , which are consistent with observed features in IRAS 15398 and L1527 (e.g., Sakai et al. 2009, 2010; Araki et al. 2017; Higuchi et al. 2018). On the other hand, the abundances of most gaseous COMs at $r \leq 100$ AU regions are lower than 10^{-9} due to slow thermal migration and thermal desorption, so few COMs have been detected in prototypical WCCC sources as L1527 and IRAS 15398. Overall, the scarcity of COMs in prototypical WCCC sources may be because that the temperature in the innermost protostellar envelopes has not reached lower limit required to motivate hot corino chemistry. Meanwhile, this also suggests that the high cosmic ray ionization rate and the long contraction timescale of the protostar are favorable physical pa-

rameters responsible for the chemical characteristics in the prototypical WCCC sources.

5.2. Differences between different gas-phase networks

Only a small portion of the reactions included in currently available public networks (e.g., KIDA and UDFA) have been investigated either in the laboratory or theoretically, leading to a significant overall level of uncertainty. Tinacci et al. (2023) used quantum mechanics calculations and found that only 5% of the reactions in the KIDA2014 database, which were previously assumed to be barrierless, are actually endothermic. After removing these endothermic reactions, they found that there was only a minor change to the abundance of most species, except for some Si-bearing species. As such, this treatment is not likely to significantly change our results. Recently, Millar et al. (2023) released the sixth version of the UDFA network, which includes more species and reactions compared to the last release. However, due to limited advancements in carbon-chain molecules, we continue to compare the UDFA12 with the KIDA2014 gas-phase network used in this work.

There are some differences between the UDFA and KIDA networks in several aspects. The KIDA network has a larger and more comprehensive network, which can be combined with some grain-surface reactions to study chemistry in planetary atmospheres (Millar et al. 2023). The KIDA network includes many unmeasured ion-neutral reactions, while the UDFA network relies more on detected molecules and well-studied reactions (Wakelam et al. 2012; Millar et al. 2023). Additionally, there are differences in approaches to estimating rate coefficients, as well as the choice of experimental rate coefficients (Wakelam et al. 2012). These differences lead to variations in the carbon-chain chemistry in typical dark clouds as simulated by Wakelam et al. (2012) and McElroy et al. (2013).

Considering the dominance of the WCCC mechanism in carbon-chain molecules in the protostellar cores, we analyzed the key reactions associated with WCCC to assess the impact of the differences between these two networks on our simulated results. The WCCC begins with gas-phase reactions of gaseous CH_4 molecules with C^+ ions, followed by a series of subsequent reactions. The reactions involving the precursor CH_4 molecules and C^+ ions in the two networks have some differences, leading to variations in the subsequent WCCC reactions. Both networks include identical reactions involving CH_4 and C^+ to produce C_2H_2^+ and C_2H_3^+ , as well as crucial formation reactions of C_2H and C_2H_2 molecules. However, there is a significant discrepancy in reaction 5 between these two networks. The rate coefficient for the reaction 5 associated with C_2H_2 in the KIDA network is expressed by $1.14 \times 10^{-11} \exp(-1300/T) \text{ cm}^3 \text{ s}^{-1}$, whereas the rate coefficient in the UDFA network is calculated by $9.11 \times 10^{-13} (T/300)^{2.57} \exp(-130/T) \text{ cm}^3 \text{ s}^{-1}$. For instance, at a temperature of 150 K, the former rate coefficient is $1.96 \times 10^{-15} \text{ cm}^3 \text{ s}^{-1}$, whereas the latter rate coefficient is $6.45 \times 10^{-14} \text{ cm}^3 \text{ s}^{-1}$. On the other hand, the UDFA network does not include reaction 5 related to C_nH ($n > 2$). Hence the dip structure of C_nH would not appear in models using the UDFA network. The UDFA network also lacks the crucial formation reactions 6 of HC_{2n+1}N ($n = 2, 3, 4$) in hot environments. In general, one can expect some differences in abundances of carbon-chain molecules using the UDFA gas-phase network. However, the spatial structures of HC_{2n+1}N and C_{2n}H_2 would not undergo significant changes as these features are determined by the evaporation temperatures.

The impact of several crucial physical parameters (i.e., A_V^{amb} , ζ , T_{max} , and t_{cont}) on WCCC has been explored using the KIDA network in Sect. 4. Does the differences between the KIDA and UDFA network directly impact our understanding of WCCC? Ultraviolet photons have a primary influence on WCCC processes through the CO photodissociation reaction, as discussed in Sect. 4.1. Since both networks have the same CO photodissociation rates, so their differences would not change the impact of UV photons on WCCC. Similarly, the direct and induced ionization reactions due to cosmic-rays for CO and CH₄ molecules are essentially the same in both networks. Therefore, one can expect similar conclusions about the influence of cosmic rays on WCCC using the UDFA network, as shown by Kalvāns (2021). The majority of gas-phase reactions governing WCCC are similar in both networks, so they may have comparable effects on WCCC when changing T_{max} and t_{cont} with different effective durations. Regarding hot corino chemistry, since most COMs are mainly dominated by surface reactions, the variations in these two gas-phase networks would not clearly impact our understanding of hot corino chemistry in this work.

5.3. Uncertainties in physical models and evolutionary timescales

Besides the treatment of the gas-phase network, there are some uncertainties in the physical models of core evolution and the timescales for various stages, which have the potential to impact the simulated results of WCCC and hot corino chemistry. Numerous works have studied the chemistry or the dynamics in prestellar cores using various physical models, including the Larson-Penston collapse model (Aikawa et al. 2001), Bonnor-Ebert sphere model (Lee et al. 2004), hydrostatic model (Masunaga & Inutsuka 2000), isothermal collapse model (Keto & Caselli 2010), free-fall collapse model (Sun & Du 2022), and magnetohydrodynamic model (Ciolek & Basu 2000). From the perspective of the chemistry, these physical models primarily differ in two important physical quantities: the number density and the visual extinction. For example, in Sun & Du (2022)'s work, the average density of clouds is lower than that in our physical model, resulting in a slow chemical evolution. However, due to significant depletion of most molecules in the late stages, as observed in Hirota et al. (2009), there is no significant difference in the abundance of precursor CH₄ and radicals adsorbed onto dust grains. Hence this would not significantly change the subsequent characteristics of WCCC and hot corino chemistry in the protostellar core. For instance, Kalvāns (2021) used a single-point collapse model, and obtained similar effects of cosmic rays on WCCC. Analogously, Aikawa et al. (2020) got similar role of the interstellar fields on WCCC and hot corino chemistry in protostellar cores, using the hydrostatic prestellar cores. The impact of variations in protostellar core models has relatively minor effects on WCCC and hot corino chemistry, mainly due to two reasons. The dynamics of inside-out collapse in the protostellar core, as simulated in several hydrodynamic (Masunaga & Inutsuka 2000) and even magnetohydrodynamic models (Tomida et al. 2010), bears resemblance to the expansion wave collapse model in this work. For instance, the density profile near the center in Aikawa et al. (2008) is close to that we used. Another important reason is that carbon-chain molecules and COMs in the protostellar envelope is more dependent on the dust temperature than the number density.

There are also uncertainties in the timescales of various evolutionary stages, including the prestellar phase, the isothermal collapse phase, the warm-up phase, and the hot corino phase.

Differences in the average density and dynamics of molecular clouds can lead to variations in the lifetimes of prestellar cores (Ward-Thompson et al. 2007; Evans et al. 2009). To understand the impact of variations in the prestellar timescale on the simulated results, we conducted additional models by adopting different retardation factors B (1.0, 0.7, 0.5, and 0.3) for the prestellar core to determine their timescales t_{pre} (corresponding to 0.5, 0.7, 1.0, and 1.7 Myr, respectively). Our models suggest that WCCC and hot corino chemistry are boosted as t_{pre} increases, which align with the simulated results reported by Aikawa et al. (2020). Due to the similar dynamics and the relatively short timescale during the isothermal collapse phase (Larson 1969; Masunaga & Inutsuka 2000; Lee et al. 2004), the impact of timescale variations on WCCC and hot corino chemistry can be considered negligible. The differences in warm-up timescales can strongly affect WCCC and hot corino chemistry, as extensively studied in Sect. 4.4. To some extent, this is also an important factor contributing to the chemical differences between low-mass and high-mass protostellar cores. As for the effect of hot corino timescale, we can perform a simple analysis by referring to Figs. 4 and 5. During the hot corino stage, the chemical characteristics of carbon-chain molecules and COMs gradually weaken over time, making it difficult to observe these molecules in the case of extended hot corino timescales. On another note, this explains why all currently discovered WCCC and hot corino sources are located in Class 0/I phases.

6. Conclusions

In this paper, we explored possible reasons for chemical differences between WCCC sources and hot corino sources, and explained the scarcity of COMs in the prototypical WCCC sources. Our conclusions are as follows:

1. Based on the spatial distribution of unsaturated carbon-chain molecules, they are divided into two types: extended distribution and a small central dip around the protostar (e.g., C_{*n*}H group), central condensation (e.g., HC_{2*n*+1}N, and C_{2*n*}H₂ groups). The appearance of the small central dip around the protostar for C_{*n*}H group is primarily dominated by the destruction reactions: C_{*n*}H + H₂ → C_{*n*}H₂ + H in the compact central regions. Most COMs exhibit flat abundance profiles in inner regions, which is because infall timescales of gas parcels through hot corino regions are shorter than the destruction timescales of COMs.
2. Our fiducial model calculated abundant carbon-chain molecules and COMs, suggesting that WCCC and hot corino chemistry can coexist in some protostars. Additionally, this model reproduced canonical characteristics of WCCC and hot corino chemistry in the hybrid source L483.
3. Strong UV photons (i.e., in the case of low the visual extinction of ambient clouds A_V^{amb}) can rapidly dissociate CO molecules, producing abundant C⁺ ions, which accelerates WCCC processes and enhances WCCC characteristics. At a high A_V^{amb} , scarce UV photons weaken the dissociation of COMs and their precursors, enhancing hot corino chemistry features. Therefore, UV photons heighten the WCCC features by accelerating the photodissociation of CO molecules, while they weaken the hot corino features. This explains the statistical characteristics of observations, where WCCC sources are often found at the cloud boundaries, while hot corino sources tend to be located inside dense clouds.
4. Another physical parameter in local environments - the cosmic-ray ionization rate (ζ) can also lead to differences in

WCCC, but the response of hot corino chemistry to ζ variation is highly species-dependent. Intensive cosmic rays accelerate the dissociation of CO and CH₄ molecules, generating abundant C⁺ ions, which enhances the WCCC characteristics. The influence of cosmic rays on hot corino chemistry is relatively complex, which is mainly because that COMs and their precursors are affected by various reactions associated with cosmic rays.

5. The maximum temperature at the warm-up phase (T_{\max}) cannot affect WCCC features, while its influence varies for different COMs. It is one reason for the weak relation between the luminosity of the protostar and the abundance of COMs, as well as the kind of species. Overall, the variation of T_{\max} cannot explain the chemical differences between WCCC sources and hot corino sources. The long contraction timescale (t_{cont}) promotes WCCC and hot corino chemistry, by prolonging the effective duration of WCCC reactions in the gas phase and surface reactions of COMs, respectively. This suggests that the variation of t_{cont} can generate chemical differences between WCCC sources and hot corino sources to some extent.
6. To explain the scarcity of COMs in prototypical WCCC sources (e.g., L1527, and IRAS 15398), we adopted $\zeta = 3 \times 10^{-16} \text{ s}^{-1}$ and $t_{\text{cont}} = 5 \times 10^5 \text{ yr}$. When the temperature in the innermost layers is only about 55 K, we reproduce the chemical characteristics (i.e., scarce COMs and abundant carbon-chain molecules) in prototypical WCCC sources. Hence, we suggest that scarce COMs in prototypical WCCC sources can be attributed to the insufficient dust temperature in the innermost envelopes to trigger hot corino chemistry. Furthermore, we propose that the high ζ and the long t_{cont} also are crucial physical parameters responsible to shape scarce COMs in the prototypical WCCC sources.

Acknowledgements. We are extremely grateful to the anonymous referee for critical and constructive comments that greatly improved the original manuscript. We thank Wasim Iqbal and Rong Ma for helpful discussions and valuable comments. F.D. acknowledges the support from the National Natural Science Foundation of China, grant No. 11873094 and 12041305. Y.W. acknowledges the support by the Natural Science Foundation of Jiangsu Province (Grant Number BK20221163). The Taurus High Performance Computing system of Xinjiang Astronomical Observatory was used in our simulations.

References

- Agúndez, M., Cernicharo, J., de Vicente, P., et al. 2015a, *A&A*, 579, L10
 Agúndez, M., Cernicharo, J., & Guélin, M. 2015b, *A&A*, 577, L5
 Agúndez, M., Marcelino, N., Cernicharo, J., Roueff, E., & Tafalla, M. 2019, *A&A*, 625, A147
 Aikawa, Y., Furuya, K., Yamamoto, S., & Sakai, N. 2020, *ApJ*, 897, 110
 Aikawa, Y., Ohashi, N., Inutsuka, S.-i., Herbst, E., & Takakuwa, S. 2001, *ApJ*, 552, 639
 Aikawa, Y., Wakelam, V., Garrod, R. T., & Herbst, E. 2008, *ApJ*, 674, 984
 Al-Halabi, A. & van Dishoeck, E. F. 2007, *MNRAS*, 382, 1648
 Allen, M. & Robinson, G. W. 1977, *ApJ*, 212, 396
 Andersson, S. & van Dishoeck, E. F. 2008, *A&A*, 491, 907
 Araki, M., Takano, S., Sakai, N., et al. 2017, *ApJ*, 847, 51
 Barone, V., Latouche, C., Skouteris, D., et al. 2015, *MNRAS*, 453, L31
 Belloche, A., Maury, A. J., Maret, S., et al. 2020, *A&A*, 635, A198
 Bergin, E. A. & Tafalla, M. 2007, *ARA&A*, 45, 339
 Bernasconi, P. A. & Maeder, A. 1996, *A&A*, 307, 829
 Bertin, M., Fayolle, E. C., Romanzin, C., et al. 2013, *ApJ*, 779, 120
 Bianchi, E., Codella, C., Ceccarelli, C., et al. 2019, *MNRAS*, 483, 1850
 Bohlin, R. C., Savage, B. D., & Drake, J. F. 1978, *ApJ*, 224, 132
 Bottinelli, S., Ceccarelli, C., Lefloch, B., et al. 2004a, *ApJ*, 615, 354
 Bottinelli, S., Ceccarelli, C., Neri, R., et al. 2004b, *ApJ*, 617, L69
 Bottinelli, S., Ceccarelli, C., Williams, J. P., & Lefloch, B. 2007, *A&A*, 463, 601
 Bouvier, M., Ceccarelli, C., López-Sepulcre, A., et al. 2022, *ApJ*, 929, 10
 Bouvier, M., López-Sepulcre, A., Ceccarelli, C., et al. 2020, *A&A*, 636, A19
 Caux, E., Kahane, C., Castets, A., et al. 2011, *A&A*, 532, A23
 Cazaux, S., Tielens, A. G. G. M., Ceccarelli, C., et al. 2003, *ApJ*, 593, L51
 Ceccarelli, C. 2004, in *Astronomical Society of the Pacific Conference Series*, Vol. 323, *Star Formation in the Interstellar Medium: In Honor of David Hollenbach*, ed. D. Johnstone, F. C. Adams, D. N. C. Lin, D. A. Neufeld, & E. C. Ostriker, 195
 Ceccarelli, C., Caselli, P., Fontani, F., et al. 2017, *ApJ*, 850, 176
 Ceccarelli, C., Codella, C., Balucani, N., et al. 2023, in *Astronomical Society of the Pacific Conference Series*, Vol. 534, *Astronomical Society of the Pacific Conference Series*, ed. S. Inutsuka, Y. Aikawa, T. Muto, K. Tomida, & M. Tamura, 379
 Chahine, L., López-Sepulcre, A., Neri, R., et al. 2022, *A&A*, 657, A78
 Chuang, K. J., Fedoseev, G., Qasim, D., et al. 2018, *ApJ*, 853, 102
 Ciolek, G. E. & Basu, S. 2000, *ApJ*, 529, 925
 Crimier, N., Ceccarelli, C., Maret, S., et al. 2010, *A&A*, 519, A65
 Dame, T. M. & Thaddeus, P. 1985, *ApJ*, 297, 751
 Draine, B. T. 1978, *ApJS*, 36, 595
 Draine, B. T. & Bertoldi, F. 1996, *ApJ*, 468, 269
 Du, F. 2021, *Research in Astronomy and Astrophysics*, 21, 077
 Dupuy, R., Bertin, M., Féraud, G., et al. 2017, *A&A*, 603, A61
 Evans, Neal J., I., Dunham, M. M., Jørgensen, J. K., et al. 2009, *ApJS*, 181, 321
 Froebrich, D. 2005, *ApJS*, 156, 169
 Garrod, R. T. 2013, *ApJ*, 765, 60
 Garrod, R. T. & Herbst, E. 2006, *A&A*, 457, 927
 Garrod, R. T. & Pauly, T. 2011, *ApJ*, 735, 15
 Garrod, R. T., Wakelam, V., & Herbst, E. 2007, *A&A*, 467, 1103
 Garrod, R. T., Widicus Weaver, S. L., & Herbst, E. 2008, *ApJ*, 682, 283
 Graninger, D. M., Wilkins, O. H., & Öberg, K. I. 2016, *ApJ*, 819, 140
 Habing, H. J. 1968, *Bull. Astron. Inst. Netherlands*, 19, 421
 Hama, T., Kuwahata, K., Watanabe, N., et al. 2012, *ApJ*, 757, 185
 Hasegawa, T. I. & Herbst, E. 1993, *MNRAS*, 263, 589
 Hasegawa, T. I., Herbst, E., & Leung, C. M. 1992, *ApJS*, 82, 167
 Hassel, G. E., Herbst, E., & Garrod, R. T. 2008, *ApJ*, 681, 1385
 He, J., Emtiaz, S., & Vidal, G. 2018, *ApJ*, 863, 156
 He, J., Shi, J., Hopkins, T., Vidal, G., & Kaufman, M. J. 2015, *ApJ*, 801, 120
 Herbst, E. & van Dishoeck, E. F. 2009, *ARA&A*, 47, 427
 Higuchi, A. E., Sakai, N., Watanabe, Y., et al. 2018, *ApJS*, 236, 52
 Hirota, T., Ohishi, M., & Yamamoto, S. 2009, *ApJ*, 699, 585
 Hocuk, S., Szűcs, L., Caselli, P., et al. 2017, *A&A*, 604, A58
 Hollenbach, D. J., Takahashi, T., & Tielens, A. G. G. M. 1991, *ApJ*, 377, 192
 Imai, M., Oya, Y., Sakai, N., et al. 2019, *ApJ*, 873, L21
 Imai, M., Sakai, N., Oya, Y., et al. 2016, *ApJ*, 830, L37
 Indriolo, N., Blake, G. A., Goto, M., et al. 2010, *ApJ*, 724, 1357
 Indriolo, N. & McCall, B. J. 2012, *ApJ*, 745, 91
 Jacobsen, S. K., Jørgensen, J. K., Di Francesco, J., et al. 2019, *A&A*, 629, A29
 Jiménez-Serra, I., Vasyunin, A. I., Caselli, P., et al. 2016, *ApJ*, 830, L6
 Jørgensen, J. K., Belloche, A., & Garrod, R. T. 2020, *ARA&A*, 58, 727
 Jørgensen, J. K., Bourke, T. L., Myers, P. C., et al. 2005, *ApJ*, 632, 973
 Jørgensen, J. K., Schöier, F. L., & van Dishoeck, E. F. 2002, *A&A*, 389, 908
 Jørgensen, J. K., van der Wiel, M. H. D., Coutens, A., et al. 2016, *A&A*, 595, A117
 Jørgensen, J. K., Visser, R., Sakai, N., et al. 2013, *ApJ*, 779, L22
 Kalvāns, J. 2018, *MNRAS*, 478, 2753
 Kalvāns, J. 2021, *ApJ*, 910, 54
 Kalvāns, J., Shmeld, I., Kalnín, J. R., & Hocuk, S. 2017, *MNRAS*, 467, 1763
 Karska, A., Herczeg, G. J., van Dishoeck, E. F., et al. 2013, *A&A*, 552, A141
 Karssemeijer, L. J. & Cuppen, H. M. 2014, *A&A*, 569, A107
 Keto, E. & Caselli, P. 2010, *MNRAS*, 402, 1625
 Kristensen, L. E., van Dishoeck, E. F., Bergin, E. A., et al. 2012, *A&A*, 542, A8
 Kristensen, L. E., van Dishoeck, E. F., van Kempen, T. A., et al. 2010, *A&A*, 516, A57
 Kuan, Y.-J., Huang, H.-C., Charnley, S. B., et al. 2004, *ApJ*, 616, L27
 Larson, R. B. 1969, *MNRAS*, 145, 271
 Lee, C.-F., Codella, C., Li, Z.-Y., & Liu, S.-Y. 2019, *ApJ*, 876, 63
 Lee, J.-E., Bergin, E. A., & Evans, Neal J., I. 2004, *ApJ*, 617, 360
 Lefloch, B., Bachiller, R., Ceccarelli, C., et al. 2018, *MNRAS*, 477, 4792
 Li, X., Heays, A. N., Visser, R., et al. 2013, *A&A*, 555, A14
 Lindberg, J. E., Charnley, S. B., & Cordiner, M. A. 2016, *ApJ*, 833, L14
 Lindberg, J. E., Charnley, S. B., Jørgensen, J. K., Cordiner, M. A., & Bjerkeli, P. 2017, *ApJ*, 835, 3
 Loomis, R. A., Cleaves, L. I., Öberg, K. I., et al. 2018, *ApJ*, 859, 131
 López-Sepulcre, A., Sakai, N., Neri, R., et al. 2017, *A&A*, 606, A121
 Marcelino, N., Agúndez, M., Cernicharo, J., Roueff, E., & Tafalla, M. 2018a, *A&A*, 612, L10
 Marcelino, N., Gerin, M., Cernicharo, J., et al. 2018b, *A&A*, 620, A80
 Maret, S., Ceccarelli, C., Tielens, A. G. G. M., et al. 2005, *A&A*, 442, 527
 Martín-Doménech, R., Manzano-Santamaría, J., Muñoz Caro, G. M., et al. 2015, *A&A*, 584, A14
 Masunaga, H. & Inutsuka, S.-i. 2000, *ApJ*, 531, 350
 McElroy, D., Walsh, C., Markwick, A. J., et al. 2013, *A&A*, 550, A36

- Millar, T. J., Walsh, C., Van de Sande, M., & Markwick, A. J. 2023, arXiv e-prints, arXiv:2311.03936
- Minissale, M., Congiu, E., & Dulieu, F. 2016a, A&A, 585, A146
- Minissale, M., Dulieu, F., Cazaux, S., & Hocuk, S. 2016b, A&A, 585, A24
- Molinari, S., Brand, J., Cesaroni, R., & Palla, F. 2000, A&A, 355, 617
- Murillo, N. M., van Dishoeck, E. F., van der Wiel, M. H. D., et al. 2018, A&A, 617, A120
- Myers, P. C., Bachiller, R., Caselli, P., et al. 1995, ApJ, 449, L65
- Nazari, P., van Gelder, M. L., van Dishoeck, E. F., et al. 2021, A&A, 650, A150
- Neufeld, D. A., Goicoechea, J. R., Sonnentrucker, P., et al. 2010, A&A, 521, L10
- Neufeld, D. A. & Wolfire, M. G. 2017, ApJ, 845, 163
- Öberg, K. I. & Bergin, E. A. 2021, Phys. Rep., 893, 1
- Öberg, K. I., Boogert, A. C. A., Pontoppidan, K. M., et al. 2008, ApJ, 678, 1032
- Öberg, K. I., Garrod, R. T., van Dishoeck, E. F., & Linnartz, H. 2009a, A&A, 504, 891
- Öberg, K. I., Linnartz, H., Visser, R., & van Dishoeck, E. F. 2009b, ApJ, 693, 1209
- Öberg, K. I., van Dishoeck, E. F., & Linnartz, H. 2009c, A&A, 496, 281
- Ohashi, N., Hayashi, M., Ho, P. T. P., & Momose, M. 1997, ApJ, 475, 211
- Oya, Y., Sakai, N., Watanabe, Y., et al. 2017, ApJ, 837, 174
- Padovani, M., Ivlev, A. V., Galli, D., & Caselli, P. 2018, A&A, 614, A111
- Penston, M. V. 1969, MNRAS, 144, 425
- Pineda, J. E., Maury, A. J., Fuller, G. A., et al. 2012, A&A, 544, L7
- Rawlings, J. M. C., Hartquist, T. W., Menten, K. M., & Williams, D. A. 1992, MNRAS, 255, 471
- Rowan-Robinson, M. 1980, ApJS, 44, 403
- Ruud, M., Loison, J. C., Hickson, K. M., et al. 2015, MNRAS, 447, 4004
- Ruud, M., Wakelam, V., & Hersant, F. 2016, MNRAS, 459, 3756
- Ruffle, D. P. & Herbst, E. 2000, MNRAS, 319, 837
- Sakai, N., Sakai, T., Hirota, T., Burton, M., & Yamamoto, S. 2009, ApJ, 697, 769
- Sakai, N., Sakai, T., Hirota, T., & Yamamoto, S. 2008, ApJ, 672, 371
- Sakai, N., Sakai, T., Hirota, T., & Yamamoto, S. 2010, ApJ, 722, 1633
- Sakai, N., Sakai, T., & Yamamoto, S. 2006, PASJ, 58, L15
- Sakai, N. & Yamamoto, S. 2013, Chemical Reviews, 113, 8981
- Scibelli, S., Shirley, Y., Vasyunin, A., & Launhardt, R. 2021, MNRAS, 504, 5754
- Shen, C. J., Greenberg, J. M., Schutte, W. A., & van Dishoeck, E. F. 2004, A&A, 415, 203
- Shu, F. H. 1977, ApJ, 214, 488
- Shu, F. H., Adams, F. C., & Lizano, S. 1987, ARA&A, 25, 23
- Sicilia-Aguilar, A., Patel, N., Fang, M., et al. 2019, A&A, 622, A118
- Spezzano, S., Bizzocchi, L., Caselli, P., Harju, J., & Brünken, S. 2016, A&A, 592, L11
- Spitzer, L. 1978, Physical processes in the interstellar medium (Wiley)
- Sun, J. & Du, F. 2022, Research in Astronomy and Astrophysics, 22, 065022
- Taniguchi, K., Herbst, E., Caselli, P., et al. 2019, ApJ, 881, 57
- Taniguchi, K., Majumdar, L., Caselli, P., et al. 2023, ApJS, 267, 4
- Taniguchi, K., Majumdar, L., Plunkett, A., et al. 2021a, ApJ, 922, 152
- Taniguchi, K., Majumdar, L., Takakuwa, S., et al. 2021b, ApJ, 910, 141
- Taniguchi, K., Saito, M., Sridharan, T. K., & Minamidani, T. 2018, ApJ, 854, 133
- Taquet, V., López-Sepulcre, A., Ceccarelli, C., et al. 2015, ApJ, 804, 81
- Tielens, A. G. G. M. & Hagen, W. 1982, A&A, 114, 245
- Tinacci, L., Ferrada-Chamorro, S., Ceccarelli, C., et al. 2023, ApJS, 266, 38
- Tomida, K., Tomisaka, K., Matsumoto, T., et al. 2010, ApJ, 714, L58
- van Dishoeck, E. F., Blake, G. A., Jansen, D. J., & Groesbeck, T. D. 1995, ApJ, 447, 760
- Visser, R., van Dishoeck, E. F., & Black, J. H. 2009, A&A, 503, 323
- Viti, S., Collings, M. P., Dever, J. W., McCoustra, M. R. S., & Williams, D. A. 2004, MNRAS, 354, 1141
- Viti, S. & Williams, D. A. 1999, MNRAS, 305, 755
- Wakelam, V., Herbst, E., Loison, J. C., et al. 2012, ApJS, 199, 21
- Wakelam, V., Loison, J. C., Herbst, E., et al. 2015, ApJS, 217, 20
- Wang, Y., Chang, Q., & Wang, H. 2019, A&A, 622, A185
- Ward-Thompson, D., André, P., Crutcher, R., et al. 2007, in Protostars and Planets V, ed. B. Reipurth, D. Jewitt, & K. Keil, 33
- Watanabe, N., Shiraki, T., & Kouchi, A. 2003, ApJ, 588, L121
- Yang, Y.-L., Sakai, N., Zhang, Y., et al. 2021, ApJ, 910, 20
- Zucconi, A., Walmsley, C. M., & Galli, D. 2001, A&A, 376, 650